# Electronic transport properties of van der Waals nanofibers of $W_6Te_6$ atomic wires

# $W_6Te_6$原子細線からなるファンデルワールスナノファイバーの電子輸送特性

Hiroshi Shimizu
清水　宏

Department of Physics, Graduate School of Science and Engineering,
Tokyo Metropolitan University

2023

# Contents

Chapter 3

Growth and Optical Properties of High-Quality 2D WTe bundle

# Chapter 1

Introduction to Transition Metal Chalcogenides

Several types of atomically thin, two-dimensional (2D), layered van der Waals (vdW) materials, such as monolayers of graphite (graphene)[1-3] and related 2D materials[4], have recently been discovered. Furthermore, by using 2D layered vdW materials as building blocks, a new group of 2D and three-dimensional (3D) functional materials called vdW heterostructures[5, 6] has been created, which has resulted in superior physical properties and potential applications. This great success has led to a similar idea for the assembly of one-dimensional (1D) vdW materials, which could generate electronic 1D, 2D, 3D, and their crossover systems. However, controlling the physical properties of aggregates of 1D vdW materials is still difficult, and their transport characteristics are yet to be revealed. To date, there have been intensive studies on carbon nanotubes (CNTs), which are representative 1D vdW materials because CNT samples are readily available on a bulk scale[7]. The structure of CNTs can be defined by their diameter and chiral angle, and as-grown samples are always a mixture of CNTs with different structures[7]. Such heterogeneous aggregates make control of their physical properties difficult, and they have exhibited 1D electron transport properties such as TLL behavior because of the weak internanotube interactions[8, 9], as observed for isolated CNTs[10-13]. Among the 1D vdW materials as potential building blocks, apart from CNTs, interest in transition metal chalcogenides (TMCs) has been growing in recent years because of their atomically narrow, uniform wire structure and superior conductivity[14-24].

A single transition-metal chalcogenide (TMC) nanowire is composed of $M_6X_6$ triangle units ($M$: transition metal atom, $X$: chalcogen atom) (Figure 1.1a). The individual nanowires form thin bundles and $M_6X_6$ bulk crystals, which have a simple monoclinic lattice, through van der Waals (vdW) interactions (Figure 1.1b). An $M_6X_6$ crystal can also form an $A_2M_6X_6$ crystal with $P6_3/m$ symmetry upon insertion of $A$ atoms ($A$: alkaline-earth or alkali metal) (Figure 1.1c and Table 1.1). The first $A_2M_6X_6$ crystals were discovered in 1980, and $M_6X_6$ crystals were subsequently reported in 1985. In addition, isolated single $M_6X_6$ nanowires were first directly visualized in 2014. Since then, research on single $M_6X_6$ nanowires and their aggregates has progressed rapidly. This chapter surveys previous reports of nanowires and bulk crystals of $M_6X_6$ and $A_2M_6X_6$.

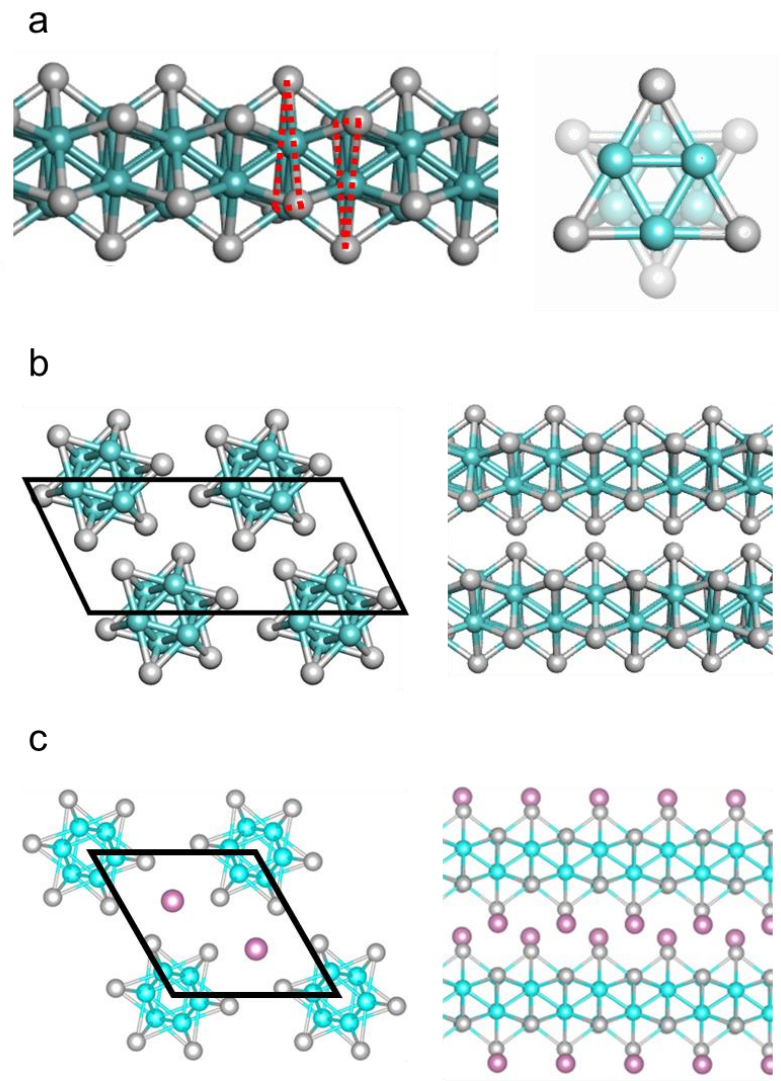


Figure 1.1 Schematics of (a) WTe nanowire composed of staggered $W_3Te_3$ triangular units. Schematics of cross-sectional (left) and side-view (right) structures of (b) $M_6X_6$ and (c) $A_2M_6X_6$. Blue, gray, and red circles correspond to $M$, $X$, and $A$ atoms, respectively.

| | | | | | | | | | | | | | | | | | |
|---|---|---|---|---|---|---|---|---|---|---|---|---|---|---|---|---|---|
| H | | $A_2M_6X_6$ | | | | | | | | | | | | | | | He |
| Li | Be | M = Transition metal X = Chalcogen | | | | | | | | | | B | C | N | O | F | Ne |
| Na | Mg | A = Intercalatied metal | | | | | | | | | | Al | Si | P | S | Cl | Ar |
| K | Ca | Sc | Ti | V | Cr | Mn | Fe | Co | Ni | Cu | Zn | Ga | Ge | As | Se | Br | Kr |
| Rb | Sr | Y | Zr | Nb | Mo | Te | Ru | Rh | Pd | Ag | Cd | In | Sn | Sb | Te | I | Xe |
| Cs | Ba | La-Lu | Hf | Ta | W | Re | Os | Ir | Pt | Au | Hg | Tl | Pb | Bi | Po | At | Rn |
| Fr | Ra | Ac-Lr | Rf | Db | Sg | Bh | Hs | Mt | Ds | Rg | Cn | Uut | Fl | Uup | Lv | Uus | Uuo |

Table 1.1 Periodic table showing the atoms that compose $M_6X_6$ and $A_2M_6X_6$.

## 1.1 $A_2M_6X_6$

### 1.1.1 Outline

$A_2M_6X_6$ was first prepared as bulk crystals in 1980 via the solid-phase growth method of heating solid raw materials [25, 26]. The physical properties of $A_2M_6X_6$ have been studied since their discovery, with a focus on superconductivity. Apart from these studies of bulk crystals, studies on the fabrication of single wires with widths of ~1 nm by solution dispersion have also attracted attention. This dispersion method has yielded nanofibers of various thicknesses from a single wire. In 2006, the relationship between the diameter of these fibers and their electron transport properties was reported[15]. Measurements of the diameter-dependent conductance of the fibers show that their conductance increases with decreasing temperature and exhibits Fermi liquid-like behavior similar to that observed in common metals in the case of crystals larger than 1 μm in diameter. However, the conductance decreases as a power of temperature, showing Tomonaga–Luttinger liquid (TLL)-like behavior characteristic of 1D metals for nanofibers with diameters of 12 nm or smaller. This result was attributed to a change in the electronic state between 3D and 1D depending on the fiber diameter, suggesting that the aggregation state of the nanofibers strongly affects their electron transport properties. Representative research cases are presented in the following sections.

### 1.1.2 Solid-phase growth of $A_2M_6X_6$

Since the synthesis of $A_2Mo_6X_6$ crystals by solid-phase growth in 1980[25, 26], numerous theoretical and experimental studies on $A_2Mo_6X_6$ crystal have been reported. Potel et al. reported the synthesis of $A_2Mo_6X_6$ crystals by annealing elements ($A$ = Tl, K, In, Na, Cs, Rb; $X$ = S, Se, Te) at 1000–1200 °C (lumps of Na, In, K, or Tl; Mo powder; and granular Se or Te under Ar)[25]. Powder X-ray diffraction (XRD) analysis revealed that the $A_2Mo_6X_6$ crystals have a hexagonal structure with space group $P6_3/m$ and that the $A$ atoms are equally spaced between $Mo_6X_6$ nanowires.

In 1980, Honle et al. also reported the synthesis of $Tl_2Fe_6Te_6$ and $A_2Mo_6X_6$ ($A$ = In, Tl; $X$ = Se, Te) crystals by heating $Mo_3X_4$ with In or Tl at 1030–1130 °C[26]. The reaction is represented by the equation $2A + Mo_3X_4 \rightarrow A_2Mo_6X_6 + AX$. X-ray analysis of the resultant crystals and powders showed that the $A_2Mo_6X_6$ structure is hexagonal with space group $P6_3/m$, consistent with the result reported by Potel et al.[25]. X-ray analysis was used to measure the lattice constants in the $a$- and $b$-axis directions perpendicular to the nanowire axis and in the $c$-axis direction parallel to the nanowire axis. The corresponding lattice constants are summarized in Table 1.2.

| | Lattice constant a, b / Å | c / Å | Reference |
|---|---|---|---|
| $Tl_2Mo_6Se_6$ | 8.94 | 4.50 | 25 |
| $K_2Mo_6S_6$ | 8.76 | 4.42 | 27 |
| $K_2Mo_6Se_6$ | 9.01 | 4.50 | 27 |
| $Cs_2Mo_6S_6$ | 8.96 | 4.46 | 27 |
| $Rb_2Mo_6S_6$ | 8.82 | 4.44 | 27 |
| $Na_2Mo_6Se_6$ | 8.74 | 4.42 | 27 |
| $In_2Mo_6Te_6$ | 9.33 | 4.59 | 26 |
| $In_2Mo_6Se_6$ | 8.84 | 4.49 | 26 |
| $Tl_2Mo_6Te_6$ | 9.42 | 4.58 | 26 |
| $Tl_2Mo_6Se_6$ | 8.92 | 4.48 | 26 |
| $Tl_2Fe_6Te_6$ | 9.35 | 4.22 | 26 |

Table 1.2 Lattice constants for $M_6X_6$, as obtained by X-ray analysis. The lengths in the directions perpendicular and parallel to the nanowire are denoted as *a* (and *b*) and *c*, respectively.

After the report of the first synthesis, Armici and Potel et al. observed superconductivity in a $Tl_2Mo_6Se_6$ crystal[28]. Electrical transport measurements showed a sharp decrease in resistance at temperatures less than 3 K. The resistance of the $Tl_2Mo_6Se_6$ crystal increased rapidly when a magnetic field of ~0.1 T was applied perpendicular to the nanowire axis. Magnetoresistance measurements showed that the critical field was largest when the magnetic field penetrated in the direction parallel to the nanowire axis. In addition, the calculated coherence length was 7.8 nm in the direction perpendicular to the nanowire axis, whereas the coherence length was 203 nm in the direction parallel to the nanowire axis. From these results, they concluded that the Fermi surface of the $Tl_2Mo_6Se_6$ crystal was anisotropic and that the sample was of high quality.

Petrovic et al. focused on changes in the electronic transport properties and energy bands depending on the type and disorder of *A* atoms in $A_2M_6X_6$ crystals. In 2010, they reported on the electronic structure and electrical transport properties of needle-shaped $A_2Mo_6Se_6$ (*A* = Tl, In, Rb) crystals with dimensions of approximately 4 mm × 300 μm × 100 μm and a mass of 800 μg[29]. Electron transport measurements revealed that $Rb_2Mo_6Se_6$ exhibits a metal–insulator transition at 170 K, whereas $Tl_2Mo_6Se_6$ and $In_2Mo_6Se_6$ undergo a metal–superconductor transition at 4.2 and 2.85 K, respectively. Local-density approximations (LDA) calculations showed that the out-of-plane dispersion of the

energy band of $A_2Mo_6Se_6$ ($A$ = Tl, In, Rb) is almost unchanged, whereas the in-plane dispersion is decreased by one-tenth for $Rb_2Mo_6Se_6$ (0.02 eV) compared with those for $Tl_2Mo_6Se_6$ (0.17 eV) and $In_2Mo_6Se_6$ (0.14 eV). From these results, Petrovic et al. considered that the change in in-plane dispersion determines the metal–insulator and metal–superconductor transitions in $A_2M_6X_6$. In 2016, they also investigated the dependence of the electron transport properties of $Na_{2-\delta}Mo_6Se_6$ crystals on structural disorder[30]. $Na_2Mo_6Se_6$ was prepared via solid-state synthesis by heating $MoSe_2$, InSe, Mo, and NaCl powders at 1000 °C for 10 h. This high-temperature reaction produced $Na_{2-\delta}Mo_6Se_6$ ($0 < \delta < 0.3$) crystals with different concentrations and locations of $Na^+$ vacancies in each sample. Electron transport measurements showed that the $Na_{2-\delta}Mo_6Se_6$ crystals exhibit metallic behavior, where their resistance decreases with decreasing temperature from 300 to 100 K. However, these measurements revealed that the resistance increases with decreasing temperature from 100 to 6 K, indicating variable-range hopping (VRH) behavior. In addition, Petrovic et al. observed that these crystals exhibit superconducting behavior, with a sharp decrease in resistance at ~6 K. The sample dependence of the metal–VRH transition temperature and VRH–superconducting transition temperature suggests that the disorder of $Na^+$ defects determine these transition temperatures.

Gannon et al. investigated the lattice dynamics of $A_2Mo_6Se_6$ ($A$ = K, Rb, Cs, In, Tl) crystals using inelastic x-ray scattering, Raman spectroscopy, and ab initio calculations[31]. These crystals were prepared using the method reported by Potel et al[25]. Gannon et al. found that the calculated structure factor and phonon frequencies of $A_2Mo_6Se_6$ crystals agreed with the experimentally determined values.

Nakayama et al. characterized $Tl_2Mo_6Se_6$ crystals using high-resolution angle-resolved photoemission spectroscopy[32]. The crystals were prepared by heating Tl shot and Mo and Se powders. The measurements showed that the $Tl_2Mo_6Se_6$ crystals have an asymmetric Dirac-like energy band and that a power-law-like suppression of the density of states (DOS) occurs near the Fermi energy. From these results, they predicted that $Tl_2Mo_6Se_6$ crystals are potential 1D topological superconductors.

Wang et al. found that $Tl_2Fe_6Te_6$ crystals exhibit a first-order paramagnetic-to-ferromagnetic phase transition at 220 K[33]. They prepared $Tl_2Fe_6Te_6$ crystals by heating Tl, Fe, and Te at 800 °C for 5 days, pulverizing the synthesized crystals, and then heating the pulverized crystals at 650 °C for 5 days. They found that the $Tl_2Fe_6Te_6$ crystals exhibit a ferromagnetic transition with decreasing temperature.

Guo et al. studied the control of electronic properties by varying the average and local structure of $A_2M_6X_6$ crystals[34]. Specifically, they compared $K_2V_6Se_6$ and $A_2V_6X_6O_x$ ($A$ = K, Rb, Cs; $X$ = Se,Te) crystals synthesized by a conventional solid-state reaction. XRD analysis showed that, in $A_2V_6X_6O_x$ crystals, O atoms occupy the center of the oxygen-free $V_6$ cluster octahedra, whereas $K_2V_6Se_6$ crystals are oxygen-free. X-ray analysis revealed that $K_2V_6Se_6$ crystals are locally highly vertically distorted at room temperature, undergoing a change in symmetry of their average structure from hexagonal $P6_3/m$ to monoclinic $P2_1/m$. Density functional theory (DFT) calculations suggested that the symmetry

of the $K_2V_6Se_6$ crystals is further distorted to $P2_1$ or $P2_1/c$ at low temperatures. Temperature-dependent resistivity measurements showed that $K_2V_6Se_6$ exhibits metallic behavior and that $K_2V_6Te_6O_{0.66}$, $Rb_2V_6Te_6O_{0.64}$, and $Cs_2V_6Te_6O_{0.7}$ undergo a metal–semiconductor–metal transition. On the basis of these results, Guo et al. attributed this transition to changes in the local structure due to oxygen atoms.

Tessema et al. reported on the electrical properties of $Tl_2Mo_6Se_6$ crystals under uniaxial stress[35]. Electrical transport measurements revealed that stress suppresses the superconducting transition temperature and induces a metal-to-nonmetal phase transition. This transition is expected to arise from the charge-density or spin-density wave observed in $K_{0.3}MoO_3$ and TaS. The corresponding strain–temperature phase diagram showed that, under low strain, a $Tl_2Mo_6Se_6$ crystal is a superconductor at low temperatures and a metal at high temperatures. This diagram also revealed that $Tl_2Mo_6Se_6$ is a semiconductor under high strain.

Tseng et al. studied the effect of uniaxial stress on the thermopower for $Tl_2Mo_6Se_6$ crystals[36]. Their results showed that the thermopower decreases when uniaxial stress greater than 0.60% is applied. On the basis of these results, they expected $Tl_2Mo_6Se_6$ to undergo a metal–insulator phase transition under uniaxial stress.

Zhang et al. investigated the electronic and transport properties of 2D monolayers and 1D nanowires of $I_2Ga_6Te_6$ using ab initio calculations, which showed that $I_2Ga_6Te_6$ has a 3D bulk, a 2D monolayer, and a 1D nanochain morphology[37]. Calculation of the corresponding band structures revealed that 3D crystalline and 2D monolayer $I_2Ga_6Te_6$ are semiconductors with an indirect bandgap of 1.82 and 1.98 eV, respectively, and that 1D nanowire $I_2Ga_6Te_6$ is a semiconductor with a direct bandgap of 2.29 eV. The strain energy for the investigated 1D $I_2Ga_6Te_6$ nanowire shows high nanowire tensile strength, which indicates superior elasticity. In addition, Zhang et al. showed that the bandgaps of 2D monolayer and 1D nanowire $I_2Ga_6Te_6$ decreases when strain is applied in the direction parallel to the nanowire axis, whereas the bandgap of the 2D monolayer material increases when strain is applied in the direction perpendicular to the nanowire axis.

Brusetti et al. measured the Hall effect in $Tl_2Mo_6Se_6$ crystals[38]. The $Tl_2Mo_6Se_6$ used in their experiment was a ribbon-shaped crystal ~5 mm long and ~20 μm thick. The temperature dependence of the resistance revealed a superconducting transition temperature of 6.5 K for $Tl_2Mo_6Se_6$. When a magnetic field of 4 T was applied, the Hall coefficient decreased with decreasing temperature from 300 to 80 K. However, the Hall coefficient increased rapidly with decreasing temperature from 80 to 6.5 K. These results clearly show that $Tl_2Mo_6Se_6$ is a superconductor.

Davidson et al. found that $Li_2Mo_6Se_6$ crystals dissolved in *N*-methylformamide (NMF) become nematic crystals (i.e., a liquid in which the constituent molecules exhibit orientational order and no 3D positional order)[39]. Optical microscopy and small-angle X-ray-diffraction experiments showed that a nematic solution of the $Li_2Mo_6Se_6$ crystals contained suspensions of charged $Mo_6Se_6$ crystals longer than 100 nm. In addition, a dispersion of $Mo_6Se_6$ crystals was found to form discrete $Mo_6Se_6$ nanowires.

These results suggest that the $Li_2Mo_6Se_6$ crystals can be regarded as an oriented assembly of isolated $Li_2Mo_6Se_6$ nanowires.

Chew et al. used nuclear magnetic resonance (NMR) to study the electronic structure of $A_2Mo_6Se_6$ ($A$ = Li, Rb, Cs, In) crystals[40]. $In_2Mo_6Se_6$ crystals were synthesized by the method reported by Tarascon et al.[41, 42], and $A_2Mo_6Se_6$ ($A$ = Li, Rb, Cs) crystals were prepared by mixing $In_2Mo_6Se_6$ crystals with an alkali iodide and heating the mixture at 500 °C. NMR spectroscopy revealed that only $In_2Mo_6Se_6$ exhibited a large difference between the measured and calculated quadrupole coupling. The authors attributed this difference to the contribution of the *p* orbitals of In to the conduction band of $Mo_6Se_6$.

### 1.1.3 Preparation of $A_2M_6X_6$ by dispersion of solution of dissolved $A_2M_6X_6$ crystals

$A_2M_6X_6$ bulk crystals and thin bundles have also been produced by dispersing solutions of dissolved crystals since the ion exchange method was reported in 1984[43]. Tarascon et al. have reported several studies of $A_2Mo_6X_6$ bulk crystals. In 1984, they synthesized $A_2Mo_6X_6$ ($A$ = Li, Na, K, Rb, Cs) and $In_{2-x}A_xMo_6X_6$ ($0 \leq x \leq 1.8$) crystals by ion-exchange reactions of $In_2Mo_6X_6$ ($X$ = Se, Te) crystals with $A$I salts ($A$ = Li, Na, K, Rb, Cs, Cu, Ag) and LiCl[43]. $In_2Mo_6Se_6$ crystals were synthesized by heating Mo powder, Se powder, and In lumps at 1000 °C for 48 h and then at 1050 °C for 24 h, which is the same method reported by Potel et al[25]. $In_{2-x}Mo_6X_6$ crystals were prepared by mixing $In_{2-x}A_2Mo_6X_6$ and an $A$I salt, pressing the resultant mixtures into pellets, and reacting them under vacuum. These reactions are described by the equations $2In + 6Mo + 6X \rightarrow In_2Mo_6X_6$ and $In_2Mo_6X_6 + xAI \rightarrow In_{2-x}A_xMo_6X_6$, respectively. The XRD patterns for the $A_2Mo_6X_6$ crystals revealed that the distance between two $A$ atoms parallel to the *c*-axis is independent of the $A$ atom size. This suggests that the Mo–Mo bond length in a bulk crystal is determined by the balance between Mo–$X$ bond energies. In addition, the preparation of $A_2Mo_6X_6$ crystals by ion exchange revealed that, when Ag and Cu salts were used as elements providing $A$ atoms, only the Cu salt reacted to produce $Cu_2Mo_6X_6$ crystals. This is likely attributable to the strong covalent nature of the Ag–Se bond, which is, in turn, attributable to the small difference in electronegativity between Ag and Se. The results also suggest that the ease of cation exchange is related to the formation of $A_2Mo_6X_6$ crystals. Tarascon et al. also investigated the electron transport properties of $A_2Mo_6X_6$ ($A$ = K, Rb, Cs, Tl; $X$ = Se, Te) crystals[42]. Electrical transport measurement showed that $A_2Mo_6X_6$ ($A$ = K, Rb, Cs; $X$ = Se, Te) crystals changed from metals to semiconductors with decreasing temperature because of the Peierls transition. However, the measurements also showed that the $Tl_2Mo_6Se_6$ crystal remains a metal and becomes a superconductor at 5.1 K. In 1985, Tarascon et al. prepared $Mo_6X_6$ ($X$ = Se, Te) nanowire solutions for the first time by exposing $A_2Mo_6X_6$ ($A$ = Li, Na; $X$ = Se, Te) crystals to highly polar solvents such as dimethyl sulfoxide (DMSO) or NMF[44]. Optical microscopy, transmission electron microscopy (TEM), and light-

scattering images showed that $Mo_6X_6$ ($X$ = Se, Te) nanowires can be oriented in solution. In addition, $Mo_6Se_6$ crystals were obtained for the first time[45]. To prepare $Mo_6Se_6$ crystals, Tarascon et al. first synthesized $In_2Mo_6Se_6$ crystals by heating In, Mo, and Se powders at 1100 °C and then oxidized the $In_2Mo_6Se_6$ crystals at 420 °C. Scanning electron microscopy (SEM) images showed $Mo_6Se_6$ bulk crystals ~10 μm long and ~20 μm wide and wool-ball aggregates of $Mo_6Se_6$ crystals greater than 20 μm in diameter. Tarascon et al. also fabricated storage batteries using $Mo_6Se_6$ crystals (cathode) and $Li_2Mo_6Se_6$ crystals (anode). The discharge curves for the devices revealed that only 10% degradation occurred after 10 recharges of the batteries. They concluded that binary and ternary TMCs can be used as Li-battery electrode materials.

Venkataraman et al. reported the fabrication and electronic properties of ultrafine bundles prepared from $Li_2Mo_6Se_6$. In 1999, they characterized the structures and electronic properties of these bundles[14]. To prepare the bundles, they synthesized $Li_2Mo_6Se_6$ crystals using the method reported by Potel et al.[25] and Honle et al.[26] and subsequently dissolved the crystals in an organic solvent. Atomic force microscopy (AFM) images revealed that the bundles were 1 nm in diameter and greater than 5 μm in length. AFM images also showed that the bundles maintained their linear structure over several microns despite their small diameter. In addition, Venkataraman et al. found that that bundles with a diameter greater than 15 nm could be produced by increasing the concentration of nanowires in dispersions. Scanning tunneling microscopy (STM) revealed that the lattice constant and diameter of the nanowires were 0.45 ± 0.01 nm and 0.53 ± 0.07 nm, respectively. These data agree well with the bulk $Mo_6Se_6$ lattice constant of 0.448 nm[25, 43]. STM images showed that these nanowires could be stably thinned to a thickness on the order of several unit cells. On the basis of these results, Venkataraman et al. proposed that nanowires can be used in various interesting studies, such as exploring the transition from isolated clusters to periodic 1D systems. Scanning tunneling spectroscopy (STS) of nanowires revealed steep peaks at +1.2 eV and −0.2 eV in the normalized conductance ($dI/dV$) curves; these peaks were attributed to van Hove singularities (VHS) in the DOS originating from a 1D system, indicating weak coupling between the bundles. Finally, low-temperature STM revealed that the structure and DOS of the bundles did not change at 77 or 5 K, indicating that the Peierls transition was not observed at temperatures as low as 5 K. This study facilitated the observation of the DOS in one dimension. In 2006, Venkataraman et al. observed a diameter-dependent transition from 3D to 1D electronic systems for the bundles[15]. Electron transport measurements revealed that the conductance of the bundles with diameters larger than 1 μm increases with decreasing temperature, whereas that of the bundles with diameters from 12 to 1.2 nm decreases according to a power law with temperature, $G \sim T^{\alpha}$. In addition, electrical transport studies of bundles with a diameter of 3 nm revealed $I \propto V$ at low voltages ($V << k_BT/e$) and $I \propto V^{\alpha+1}$ at high voltages in the 200–35 K range, where $k_B$ is the Boltzmann constant and $e$ is the fundamental charge. The authors explained these results on the basis of TLL theory. The dependence of the exponent $\alpha$ on the diameter of the

bundles revealed that $\alpha$ rapidly increases with decreasing bundle diameter. The results showed a crossover from a 1D TLL to a 3D Fermi liquid (FL) with increasing bundle diameter.

Sheridan et al. fabricated a network structure consisting of $Li_2Mo_6Se_6$ bundles[46]. To prepare $Li_2Mo_6Se_6$ networks, they synthesized $In_2Mo_6Se_6$ crystals by heating In, Mo, and Se at 1050 °C and then prepared $Li_2Mo_6Se_6$ by reacting $In_2Mo_6Se_6$ with LiI. $Li_2Mo_6Se_6$ networks were subsequently prepared by deposition of a DMSO or NMF solution of $Li_2Mo_6Se_6$ onto substrates or TEM grids. The reaction equations for the preparation of $In_2Mo_6Se_6$ and $Li_2Mo_6Se_6$ are $2In + 6Mo + 6Se \rightarrow In_2Mo_6Se_6$ and $In_2Mo_6Se_6 + 2LiI \rightarrow Li_2Mo_6Se_6 + 2InI$, respectively. High-angle annular dark-field scanning transmission electron microscopy (HAADF-STEM) images showed that the junctions in the $Li_2Mo_6Se_6$ network are seamlessly interwoven and continuous. AFM imaging revealed that the $Li_2Mo_6Se_6$ network structure is formed by the self-assembly of $Li_2Mo_6Se_6$ when the solvent in the $Li_2Mo_6Se_6$ solution evaporates.

Jeon et al. synthesized $Li_2Mo_6Se_6$ nanowires by ion-exchange reactions of $In_2Mo_6Se_6$ crystals, which they prepared by heating a mixture of In granules and Mo and Se powders with LiI[47]. This reaction is described by the equation $In_2Mo_6Se_6 + 2LiI \rightarrow Li_2Mo_6Se_6 + 2InI$, which is the same as that used by Tarascon et al.[43]. UV‑vis absorption spectroscopic analysis and AFM and SEM images of $Li_2Mo_6Se_6$ nanowires dispersed in water showed that several nanometers of $Mo_6Se_6$ nanowires were uniformly dispersed. Jeon et al. speculated that ion-exchange reactions involving $Li^+$ ions could be used to synthesize $Li_2Mo_6Se_6$, which can be efficiently dispersed in water, enabling the fabrication of various devices using aqueous-dispersion-based 1D $Mo_6Se_6$ nanowires.

Regarding dispersion studies, thin films, nanocomposites, and bundles of $A_2M_6X_6$ have been prepared, accompanied by theoretical calculations of interatomic bonds. Dronskowski and Hoffmann theoretically investigated the varying solubility of $A_2Mo_6X_6$ ($A$ = Li, Na, K, In; $X$ = Se, Te) crystals in polar solvents by calculating the Mo–Mo, Mo–$X$, and $A$–$X$ bond energies[48]. Their calculations showed that the Mo–Mo bonds are chemically inert and revealed that the highly acidic $A$–$X$ bonds react with bases and thus dissolve the phases containing Li and Na. In addition, their calculations suggested that the Mo–$X$ bonds can react with strong acids because of the high basicity of the Mo–$X$ bonds. Golden et al. prepared $Li_2Mo_6Se_6$ thin films and composites. In 1995, Dronskowski and Hoffmann synthesized $Li_2Mo_6Se_6$ thin films with thicknesses greater than 1 μm by coating or spin-coating a solution of $Li_2Mo_6Se_6$ dissolved in DMSO onto a substrate and then heating the coated substrate under vacuum[49]. Their experimental TEM, SEM, and XRD results revealed that the $Li_2Mo_6Se_6$ film was composed of locally arranged $Li_2Mo_6Se_6$ nanowires. Absorption polarized light microscopy showed that the $Li_2Mo_6Se_6$ nanowires were aligned over a distance of 160 μm. In addition, the resistivity of the $Li_2Mo_6Se_6$ thin films was $5 \times 10^{-3}$ Ω cm$^{-1}$ at 23 °C. In 1996, they fabricated $Li_2Mo_6Se_6$ nanocomposites consisting of $Li_2Mo_6Se_6$ nanowires[50]. Composites were prepared by dissolving $Li_2Mo_6Se_6$ nanowires in vinylene carbonate, adding a cross-linking agent, and inducing rapid

polymerization. Polymerization of this dilute solution formed $Mo_6Se_6$ mono-wires and bi-wires with a diameter of 0.6–2 nm and a length of 50–100 nm. However, polymerization of a higher-concentration solution led to nanocomposites with diameters of 2–4 nm and lengths of 1.5 μm. *Z*-contrast STEM images showed that the wires composing this nanocomposite were oriented. Polarized-visible absorbance microscopy and polarized-UV–vis transmission spectroscopy indicated that the wires are optically anisotropic. Conductivity measurements also showed that the conductivity of the composite $Li_2Mo_6Se_6$ is $10^2$–$10^3$ S $cm^{-1}$, which is comparable to that of neat $Li_2Mo_6Se_6$ thin films ($2 \times 10^2$ S $cm^{-1}$).

Osterloh et al. synthesized nanocomposites of metal-attached $Li_2Mo_6Se_6$ bundles by mixing liquid elements[51]. $Li_2Mo_6Se_6$ composites were prepared by adding a $Li_2Mo_6Se_6$ solution to a solution of CdSe particles coordinated with trioctylphosphine oxide (TOPO) and to a solution of colloidal Au particles. Electronic transport measurements showed that the nanocomposites have metallic properties, with a conductivity that increases with decreasing temperature; the measurements also showed that the specific conductivity of both nanocomposites was 1000 $\Omega^{-1}$ $cm^{-1}$ at 300 K, which is the same as that reported for pure $Li_2Mo_6Se_6$ crystals. These experimental values for the specific conductivity (100~1000 $\Omega^{-1}$ $cm^{-1}$) of the nanocomposites are consistent with the values obtained by theoretical calculations[50]. The results indicated that $Li_2Mo_6Se_6$ bundles are suitable for electrical connection of nanostructured films because the bundles could be bonded by metal particles.

Qi et al. investigated the molecular adsorption of $Li_2Mo_6Se_6$ thin films prepared by dispersion. In 2005, they reported that the conductivity of $Li_2Mo_6Se_6$ thin films decreases when the films are exposed to molecular vapor[52]. The $Li_2Mo_6Se_6$ thin films were prepared by dropping $Li_2Mo_6Se_6$ dissolved in water or DMSO onto thin (100 nm) films of indium tin oxide (or Au) on borosilicate glass and then evaporating the solvent. The electrical transport properties showed that the resistance of $Li_2Mo_6Se_6$ thin films is $(3–4) \times 10^{-3}$ Ω cm at room temperature and that the resistance increases by as much as 70% when the films are exposed to DMSO, NMF, or water molecules. In 2006, Qi et al. demonstrated that the temporal and steady-state changes in resistance for $Li_2Mo_6Se_6$ thin films exposed to vapor depend on the number of molecules adsorbed on the films[53]. They reported that the adsorption capacity and corresponding resistance of $Li_2Mo_6Se_6$ strongly depend on the polarity of the solvent, increasing in the order hexane < tetrahydrofuran < ethanol < DMSO. AFM observations of $Li_2Mo_6Se_6$ films showed that the $Li_2Mo_6Se_6$ films are composed of bundles of $Li_2Mo_6Se_6$ nanowires and revealed that vapor molecules are deposited onto the nanowire bundles, causing the $Li_2Mo_6Se_6$ film to expand by ~6% in volume. This result provided evidence that the molecular coating of $Li_2Mo_6Se_6$ bundles reduces interwire charge transport in the thin films. These results suggest that $Li_2Mo_6Se_6$ bundles are sensitive to molecular adsorption as a metal conductor, indicating that $Li_2Mo_6Se_6$ can be used as a chemical sensor.

### 1.1.4 Theoretical calculation for $A_2M_6X_6$

Brusetti et al. reported two papers on the critical field for $Tl_2Mo_6Se_6$ crystals and on the phonon DOS for $Mo_6Se_6$ and $A_2Mo_6Se_6$ ($A$ = Tl, In, Rb) crystals. In 1988, they reported low-field measurements of the superconductor $Tl_2Mo_6Se_6$[54]. The measurements revealed that the critical field for $Tl_2Mo_6Se_6$ is as low as 95 ± 15 mOe. They also studied the phonon DOS for $Mo_6Se_6$ and $A_2Mo_6Se_6$ ($A$ = Tl, In, Rb) crystals to investigate the occurrence of superconductivity[55]. To fabricate $Mo_6Se_6$ crystals, they prepared $In_2Mo_6Se_6$ crystals by the same method as Potel et al.[25]. They then removed In atoms from $In_2Mo_6Se_6$ crystals by treating the crystals in flowing HCl gas at 500 °C. They also prepared $A_2Mo_6Se_6$ crystals ($M$ = Tl, Rb) in the same manner as $In_2Mo_6Se_6$ crystals.

Several studies on the transport properties of $A_2M_6X_6$ were reported in the 1980s. Huang et al. reported the temperature and pressure dependence of the resistance of the superconductor $Tl_2Mo_6Se_6$[56]. Electrical transport measurements revealed that the electrical conductivity increased under increasing pressure and that the superconducting transition temperature was suppressed. Mori et al. evaluated the Seebeck coefficients for $Tl_2Mo_6Se_6$ and $In_2Mo_6Se_6$ crystals at 1.8 K to be −40 and −5 V $K^{-1}$, respectively, suggesting that the DOS at the Fermi level for these crystals differs[57]. Lepetit and Potel measured the transport properties for $A_2Mo_6X_6$ ($A$ = In, Tl; $X$ = Se, Te) crystals and found that only $Tl_2Mo_6Se_6$ is a superconductor and that its critical temperature is 5.5–6.6 K [58]. Hor and Tarascon et al. reported that metal–semiconductor transitions are suppressed monotonically in $Rb_2Mo_6Se_6$, $Rb_2Mo_6Te_6$, and $Cs_2Mo_6Te_6$ crystals under increasing pressure[59]. These crystals were prepared by ion exchange of $A^+$ ($A$ = Rb, Cs) for $In^+$ in $In_2Mo_6X_6$ ($X$ = Se, Te) using alkali iodides at low temperatures, which is the same approach reported previously by Tarascon et al.[41]. The resistance of $In_2Mo_6X_6$ decreased with decreasing temperature between ~100 and ~300 K; however, at temperatures less than 100 K, the resistance increased with decreasing temperature. These data indicate that the crystals undergo a metal–semiconductor transition. They also show that the resistance and the metal–semiconductor transition for these crystals were inhibited rapidly with increasing pressure at temperatures less than ~100 K. The authors described that the metal–semiconductor transition of $A_2M_6X_6$ is associated with a Peierls transition, which occurs simultaneously with lattice deformation and band-structure changes in the lattice and electron systems, respectively, in metals.

Cai et al. calculated the band structures of $Mo_6Te_6$, $Mo_6X_8$, $PbMo_6X_8$, and $Tl_2Mo_6X_6$ ($X$ = S, Se, Te) crystals by the tight-binding method with the extended Hückel approximation to investigate the relationship between the binding properties and superconducting transition temperature[60]. Their calculation results showed that the energy bands for these crystals are metallic and that Mo 4*d* states are dominant near the Fermi energy. They also showed that, apart from $Mo_6Se_8$, these crystals have similar electronic structures. The band structures revealed that their Fermi energies lie in a DOS peak, which might result in higher superconducting transition temperatures.

Durgun et al. calculated the structural, electronic, and mechanical properties of $A_2M_6X_6$ and $M_6X_6$

nanowires and $A_2M_6X_6$ ($A$ = Li, Na; $M$ = Mo, W, Cr; $X$ = S, Se, Te) bulk crystals[61]. Their ab initio calculations showed that $A_2M_6X_6$ and $M_6X_6$ can form stable nanowires consisting of staggered $M_3X_3$ lattice triangles and that these nanowires have nonmagnetic ground states. They also found that the structure of $A_2M_6X_6$ and $M_6X_6$ nanowires can be either metallic or semiconducting depending on the $X$ atom and that all $M_6X_6$ nanowires with $X$ = Te are semiconducting. In addition, ab initio calculations showed that the structures of $A_2M_6X_6$ and $M_6X_6$ nanowires are stable at high temperatures (~500 K). Their simulations further revealed the formation of strong chemisorption bonds between $Mo_6Se_6$ nanowires and H, O, and transition-metal atoms such as Cr and Ti. This suggests that $Mo_6Se_6$ nanowires can be used as functional materials. The band structure of $Li_2Cr_6Te_6$ crystals revealed that the dispersion of bands in the Γ–A direction along the nanowire axis is stronger than that along the A–L direction perpendicular to the nanowire axis. These results are consistent with the 1D nature of bulk $A_2M_6X_6$ compounds. This calculation revealed that the interaction between individual chains is weak. Band calculations for a $Li_2Cr_6Te_6$ bulk crystal also showed that alkali atoms Li and Na donate electrons to the wire, changing the number of bands crossing the Fermi energy. This doping increases the Fermi energy, resulting in metallic behavior for $Li_2Cr_6Te_6$. From these results, they found that the $Cr_6Te_6$ nanowire exhibited semiconducting behavior and that the $Li_2Cr_6Te_6$ bulk crystal exhibited metallic behavior.

Gemming et al. investigated the structure and stability of $Li_2Mo_6S_6$[62]. For the Li atoms, they investigated two arrangements: (a) decorated on the nanowire surface and (b) placed in the center of the two $Mo_3$ triangles of the chain. The calculation results showed that structure (a) is energetically more stable by 1.28 eV per Li atom than structure (b). They also revealed that the stable structure of a $Li_2Mo_6S_6$ nanowire has a diameter of 7.16 Å, an average Mo–Mo distance of 2.67 Å, and a repeat unit length of 4.36 Å. Further calculations showed that decorating Li atoms onto $Mo_6S_6$ nanowires leads to a reduction in the lattice constant $a$ perpendicular to the wire from 9.20 to 9.10 Å and to an expansion of the parallel lattice constant $c$ from 4.35 to 4.46 Å. In addition, the band structure of $Li_2Mo_6S_6$ is shifted by approximately −1 eV from that of $Mo_6S_6$. The calculations also showed that the energy band for Li (1.2–1.3 eV) exists above the Fermi energy for $Mo_6S_6$ (0.1–0.2 eV), suggesting that electrons are transferred from Li to the $Mo_6S_6$ nanowire.

Liu et al. used energy-band calculations to show that $A_2Mo_6X_6$ ($A$ = Na, K, Rb, In, Tl; $X$ = S, Se, Te) crystals can vary from Dirac semimetals to Peierls semiconductors depending on the combination of atoms[63]. Their DFT calculations showed that the space groups for $A_2Mo_6X_6$ are $P6_3/m$ and $P6/mcc$. Calculations of the energy bands revealed that $A'_2Mo_6Te_6$ ($A'$ = Rb, Tl) is a Dirac semimetal, whereas $A''_2Mo_6S_6$ and $A''_2Mo_6Se_6$ ($A''$ = Na, K, Rb) are Peierls semiconductors. The calculations also suggested that $In_2Mo_6S_6$ and $Tl_2Mo_6S_6$, $In_2Mo_6Se_6$, $Tl_2Mo_6Se_6$, $Na_2Mo_6Te_6$, and $K_2Mo_6Te_6$ can assume both semimetallic and semiconducting states.

Yang et al. investigated the band structure and mechanical properties of $A_2Mo_6S_6$ ($A$ = K, Rb, Cs)

wires using ab initio calculations[64]. Their calculations revealed that all three $A_2Mo_6S_6$ band structures are nearly identical and have semimetallic properties. Young's modulus calculations also showed that the $A_2Mo_6S_6$ nanowires exhibit strong anisotropy, with the major axis along the parallel direction of the wires.

Song et al. found by ab initio calculations that $Tl_2Mo_6Se_6$ under pressure undergoes a structural transition from the hexagonal phase to the body-centered tetragonal phase[65]. The results indicated that $Tl_2Mo_6Se_6$ can have three different structures under pressure: an orthorhombic *Cmcm* phase, a tetragonal *P*4*mm* phase, and a body-centered-tetragonal *I*4*mm* phase. Among these candidates, the *I*4*mm* phase exhibits the lowest enthalpy at pressures greater than 50 GPa. These results suggest that $Tl_2Mo_6Se_6$ undergoes a structural phase transition from the hexagonal $P6_3/m$ structure to the *I*4*mm* structure at ~50 GPa with increasing pressure.

## 1.2 $M_6X_6$

### 1.2.1 Outline

$M_6X_6$ is a simple monoclinic lattice crystal with lattice constants of approximately 8–9 Å and 4.3–4.6 Å in the directions perpendicular and parallel to the nanowire axis, respectively (Table 1.3). $M_6X_6$ was first prepared as a bulk crystal in 1985 by oxidation of $In_2Mo_6Se_6$ crystals[45]. Compared with the available fabrication methods for $A_2M_6X_6$, more varied fabrication methods have been reported for $M_6X_6$, including $H_2S$ annealing of Mo raw materials in 2008[66], electron-beam dechalcogenation of monolayer $MoSe_2$ in 2014[67], and molecular beam epitaxy in 2020[20]. These methods led to the fabrication of isolated nanowires and nanofibers consisting of several wires aggregated together, which has seldom been reported for $A_2M_6X_6$. These improvements in sample preparation methods have enabled the study of the physical properties of $M_6X_6$ specimens ranging from bulk crystals to isolated nanowires and aggregates of several nanowires. These studies have also shown that the electronic properties of $M_6X_6$ nanofibers can be tuned by their aggregation state. In fact, STS measurements in 2020 demonstrated that isolated $W_6Te_6$ nanowires are semiconductors, whereas nanofibers consisting of 2–6 nanowires are semimetals[20]. These studies show that the electronic properties of $M_6X_6$ nanofibers can be tuned via their aggregation state. Representative research cases are presented in the following sections.

| | DFT calculation | | | STM, STEM images | | |
|---|---|---|---|---|---|---|
| | Lattice constant a, b / Å | c / Å | Reference | a, b / Å | c / Å | Reference |
| $Mo_6Te_6$ | 9.02 | 4.55 | 68 | 8.9 | 4.6 | 18 |
| $Mo_6S_6$ | 7.99 | 4.34 | 68 | – | 4.4 | 17 |
| $Mo_6Se_6$ | 8.96 | 4.44 | 69 | 8.67 | 4.4 | 70 |
| $W_6Te_6$ | 9.42 | 4.56 | 69 | 9.0 | 4.45 | 71 |
| $W_6S_6$ | 9.04 | 4.35 | 69 | – | – | |
| $W_6Se_6$ | 9.12 | 4.44 | 69 | – | – | |

Table 1.3 Lattice constants for $M_6X_6$, as obtained from DFT calculations and STM and STEM images. The lengths in the direction perpendicular and parallel to the nanowire are denoted *a* (and *b*) and *c*, respectively.

## 1.2.2 Fabrication and measurements of $M_6X_6$

Kibsgaard et al. characterized the atomic-scale structure of $Mo_6S_6$ bundles using STM observations, STS measurements, and DFT calculations[16]. They synthesized $Mo_6S_6$ bundles by physical vapor deposition of Mo onto a highly ordered pyrolytic graphite (HOPG) substrate by sulfidation at 1000 K. STM observations showed that the height and the width of the $Mo_6S_6$ bundles are extremely uniform, where the height of the $Mo_6S_6$ nanowires is 0.90 ± 0.01 nm and the width of the bundles is 1.2 ± 0.2 nm. A width distribution histogram of the $Mo_6S_6$ bundles revealed that each $Mo_6S_6$ bundle is mainly composed of thre single $Mo_6S_6$ nanowires. DFT calculations showed that the structure of a $Mo_6S_6$ bundle is most stable when a $Mo_6S_6$ nanowire is rotated 60° around the nanowire axis relative to the adjacent nanowire. The DOS distribution for the trimer $Mo_6S_6$ bundles reproduced from STS spectra displayed a number of sharp peaks because of 1D VHS. Kibsgaard et al. also found that both the experimental and theoretical DOS curves for normalized conductance indicate a similar electronic structure. On the basis of these results, they demonstrated that the $Mo_6S_6$ bundle consisting of three $Mo_6S_6$ wires is indeed 1D electric conductors.

Lin et al. fabricated $M_6X_6$ ($M$ = Mo, W; $X$ = S, Se) nanowires and monolayer transition-metal dichalcogenide (TMDC) junctions at arbitrary locations[17]. Single-layer TMDCs (i.e., $MoS_2$, $MoSe_2$, and $WSe_2$) were fabricated by exfoliating bulk TMDCs crystals onto a Si substrate and transferring them to a TEM grid. The $M_6X_6$ nanowires were obtained by focusing and etching a 60 keV electron beam at any point in single-layer TMDCs observed by STEM. In situ electrical measurements showed an increase in the conductance of the $M_6X_6$ compared with that of the TMDCs. These data indicated

that the semiconductor TMDC was converted to metal nanowires. Sequential atom-resolved Z-contrast images revealed that the nanowires rotate and bend continuously while maintaining their structural integrity in response to the momentum of the electron beam. These results suggest that electron-beam technology can be used to pattern 1D conductive nanowires directly onto 2D semiconductor materials, with nanometer precision.

Zhu et al. confirmed a phase transition from $MoTe_2$ to $Mo_6Te_6$ nanowires by thermal activation at 400–500 °C[18]. $Mo_6Te_6$ nanowires were fabricated by annealing approximately 15–20 layers of $MoTe_2$ crystals under vacuum. Time-sequence images revealed that $Mo_6Te_6$ nanowires in the micrometer range were formed from $MoTe_2$ crystals. $Mo_6Te_6$ was also shown to be thermally stable even after reannealing at 450 °C. STEM images revealed that the $Mo_6Te_6$ bundle is an aggregate of monoclinic $Mo_6Te_6$ nanowires with a lattice constant of 8.9 Å and an acute angle of 58°. The STEM images also showed that each $Mo_6Te_6$ nanowire is slightly rotated by 11° and that two adjacent nanowires are axially shifted by a half-period (2.3 Å). The corresponding DFT band structures revealed that a single $Mo_6Te_6$ nanowire exhibits semiconducting behavior, with a bandgap of ~0.3 eV, whereas bulk $Mo_6Te_6$ nanowires exhibit metallic character.

Yu et al. fabricated 1D $Mo_6Te_6$ and 2D $MoTe_2$ heterostructures by molecular beam epitaxy on HOPG substrates[24]. STM images showed that $MoTe_2$ was obtained when the HOPG temperature was 250–400 °C, $Mo_6Te_6$ was obtained when the HOPG temperature was 500 °C, and both $MoTe_2$ and $Mo_6Te_6$ were obtained when the HOPG was heated to 450 °C. STM images of the $Mo_6Te_6$ also showed that the nanowire bundles became wider and thicker with increasing growth time. In addition, these images revealed that the $Mo_6Te_6$ wires were isolated when the growth time was short, whereas $Mo_6Te_6$ was densely assembled to form a network when the growth time was long. DFT calculations showed that $MoTe_2$ is a semiconductor with a bandgap of 1.1 eV and that $Mo_6Te_6$ has a bandgap greater than 50 meV, indicating that it is a semimetal.

Nagata et al. established a simple method for synthesizing isolated transition-metal monochalcogenide $Mo_6Te_6$ nanowires using carbon nanotubes (CNTs) as a mold[19]. They synthesized $Mo_6Te_6$ nanowires by vacuum annealing CNTs and $MoTe_2$ bulk crystals at 1000 °C. STEM images showed that the lattice constants measured parallel and perpendicular to the axial direction of the nanowires were 4.4 and 4.8 Å, respectively. HAADF-STEM images also revealed that $Mo_6Te_6$ nanowires confined within CNTs could be bent and twisted. Such torsion-like structural dynamics observed in single $Mo_6Te_6$ nanowires have not been reported in $Mo_6Te_6$ bundles. Therefore, this observation suggests that a single $Mo_6Te_6$ nanowire itself might have unique mechanical properties.

Slade et al. created five types of SnSe crystals, including $Sn_6Se_6$, in CNTs[72]. They fabricated SnSe wires inside CNTs by vapor-phase transport of bulk SnSe, followed by heating at ~820 °C via the sublimation method. CNTs with SnSe wires were then dispersed in ethanol and deposited onto carbon-coated Cu TEM grids. STEM images showed that five types of 1D SnSe nanocrystals were

synthesized: linear dipole chains, zig-zag chains, 2 × 1 and 2 × 2 cubes, and $Sn_6Se_6$ TMC. All of these crystals were obtained during the same encapsulation process using identical production conditions. Therefore, which SnSe structures are formed is considered to be determined by the inner diameter of the CNTs.

Xia et. al. fabricated $Mo_6Se_6$ nanowires by annealing $MoSe_2$ mono- and bi-layers[22]. STS images showed that $Mo_6Se_6$ nanowires of arbitrary length were generated at the Se-terminated zigzag edges of $MoSe_2$ and joined to $MoSe_2$ at the atomic level. They also revealed that the $Mo_6Se_6$ nanowires are metallic.

Yoo et al. synthesized ultrathin 1D $Mo_6Te_6$ wires on various substrates such as $Si_3N_4$, $SiO_2$, and doped SiC by chemical vapor deposition (CVD)[73]. They synthesized $Mo_6Te_6$ nanowires by heating Te fragments and $MoO_3$ powder and transporting them onto a substrate with Ar and $H_2$ gases. SEM images showed that dense 1D $Mo_6Te_6$ wires grew laterally on $Si_3N_4$, $SiO_2$, and doped SiC substrates to form 1D wire networks. AFM images revealed that the $Mo_6Te_6$ wires were approximately 3–5 nm thick. The electrical transport properties showed that the sheet resistance of these wires was 4.90–4.94 $k\Omega\ sq^{-1}$ at 80–300 K and that the resistivity of the wire network ranged from $4.90 \times 10^{-4}$ to $4.94 \times 10^{-4}\ \Omega$ cm. An increase in the Hall resistance was observed when the temperature was lowered from 300 to 100 K. The calculations indicated that the carrier density for the 1D $Mo_6Te_6$ wire network was $2.75\ (\pm 0.1) \times 10^{22}\ cm^{-3}$ and $4.66\ (\pm 0.27) \times 10^{22}\ cm^{-3}$ at 100 and 300 K, respectively. These results indicate that the 1D $Mo_6Te_6$ wire network exhibits metallic behavior.

Kanda et al. synthesized $Mo_6Te_6$ and $W_6Te_6$ nanowires directly within CNTs by the CVD method[21]. They prepared CNT-encapsulated $Mo_6Te_6$ and $W_6Te_6$ nanowires by vacuum annealing $MoO_x$ and $WO_x$ with Te, respectively. Raman spectra and EDS analysis identified the synthesized wires as $Mo_6Te_6$ and $W_6Te_6$. Optical absorption spectra revealed that these wires exhibit strong optical absorption peaks in the visible-light range. XPS analyses showed that the inner TMC nanowires strongly interact with the outer carbon, which leads to *n*-type doping of the TMC nanowires.

Deng et al. observed by STS observations that a single $W_6Te_6$ nanowire becomes a semiconductor[20]. They fabricated isolated $W_6Te_6$ nanowires on a bilayer graphene substrate using a bottom-up method. STS observations showed that the $W_6Te_6$ bundles of 2–6 nanowires aggregated by vdW forces are metallic, with no energy gap. However, STS observations revealed that a single $W_6Te_6$ nanowire is a semiconductor with a bandgap of 62 ± 5 mV. The results showed that bi-wire and multi-wire arrays undergo a dramatic semiconductor-to-metal transition despite their vdW interaction with weak interwire coupling. This study demonstrated that wire-by-wire vdW stacks are versatile 1D materials with tunable electronic properties.

Hong et al. fabricated 2D layered $Mo_4S_6$ and $Mo_6Se_6$ and 1D $Mo_3S_4$ in monolayer hexagonal $MX_2$ via multiphase transformations, including the $MoSe_2 \rightarrow Mo_6Se_6$ nanowire transformation[74]. Annular dark-field STEM observations showed that these multiphase transformations occurred because of in

situ heating of monolayer $MoS_2$ and $MoSe_2$ at temperatures greater than 500 °C. Hong et al. also found that these transformations are highly localized, with atomically sharp boundaries. STEM images of the $Mo_6Se_6$ growth process showed that the addition of Mo atoms to $MoSe_2$ leads to decomposition of the $MoSe_2$ and to the binding of Mo to $Mo_6Se_6$. DFT calculations revealed that $Mo_4S_6$ is a semiconductor with a bandgap of 0.86 eV and that $Mo_6Se_6$ is a metal. They also found that semiconductor–semiconductor $MoS_2$–$Mo_4S_6$ and semiconductor–metal $MoSe_2$–$Mo_6Se_6$ in-plane biphasic heterostructures have a small contact barrier of 0.24 eV and a large Schottky barrier of 0.82 eV, respectively, because $M_6X_6$ has a larger work function than other semiconducting phases. On the basis of these results, Hong et al. suggested that heterostructures can be applied to the design of heterostructure-based devices such as rectifiers and transistors.

Faulques et al. used a combination of Raman spectroscopy and DFT calculations to investigate the vibrational and electronic properties of $Sn_4Se_4$ and $Sn_6Se_6$ nanowires encapsulated in CNTs[75]. Their theoretical calculations showed that single SnSe nanowires are composed of $Sn_4Se_4$ with a square (2 × 2) atomic arrangement and $Sn_6Se_6$ with a repeating structure, similar to hexagonal $Mo_6S_6$. Raman spectra of the nanowires showed peaks attributable to $Sn_4Se_4$ (151 and 185 $cm^{-1}$) and $Sn_6Se_6$ (235 $cm^{-1}$) nanowires, supporting the theoretical predictions. The band structures revealed that $Sn_4Se_4$ nanowires are semiconducting, with an electronic gap of 1.5 eV, and that $Sn_6Se_6$ nanowires are semimetallic. The Raman spectrum of the composite SnSe in CNT showed a strongly suppressed CNT vibration, suggesting that the CNTs interacted with the encapsulated SnSe nanowires. From these results, the authors concluded that the encapsulated SnSe nanowires changed the electronic and oscillational properties of the surrounding walls of single-walled CNTs.

## 1.2.3 Theoretical calculation for $M_6X_6$

Ribeiro et al. carried out ab initio pseudopotential total energy calculations for bulk crystals and isolated nanowires using the LDA[76]. Energy-band calculations for $Li_2Mo_6Se_6$ bulk crystals, isolated MoSe nanowires, and an isolated Li-containing MoSe nanowire indicated that these systems are all metallic. Ribeiro et al. revealed that the binding energy between Li atoms and $Mo_6Se_6$ is approximately 2.5 eV per Li atom. On the basis of these results, the authors proposed that Li acts primarily as an electron donor, suggesting that other alkali atoms can also function as donors.

Vilfan et al. investigated the electronic structure of $Mo_6S_6$ nanowires using ab initio calculations based on DFT[77]. The calculations showed that $Mo_6S_6$ constructs weakly bound 1D chains such as $Mo_6Se_6$ and $Mo_6S_{9-x}I_x$ nanowires, with strong mechanical and electronic uniaxiality. DFT simulations revealed that the $Mo_6S_6$ geometry is metastable, 28 eV greater per unit lattice than the layered $MoS_2$ geometry. Vilfan et al. also found that $Mo_6S_6$ nanowires exhibit better conduction and mechanical properties than Mo–S–I nanowires such as $Mo_6S_{9-x}I_x$.

Popov et al. calculated the changes in $Mo_6S_6$ nanowires when S atoms are displaced by I atoms or

the nanowires or bent or twisted. In 2007, they reported the structural, electronic, and transport properties of $Mo_6S_{6-x}I_x$ bundles, where S atoms were partially substituted with I atoms, by calculation of ab initio density functional and quantum transport in the nonequilibrium Green's function form[78]. Compared with the calculated Mo–Mo bond length and the lattice constant for $Mo_6S_6$ bundles, those for $Mo_6I_6$ bundles are 0.01 nm and 0.021 nm greater, respectively. The average binding energy revealed that, among the investigated $Mo_6S_{6-x}I_x$ bundles, $Mo_6S_4I_2$ bundles with a symmetrical arrangement of I atoms are the most stable and $Mo_6I_6$ bundles are the most unstable. Calculations of the band structure revealed that the band structures for both the $Mo_6S_6$ and $Mo_6S_4I_2$ have a Dirac cone-like shape near the Fermi level. They also revealed that the $Mo_6S_4I_2$ bundles are semiconductors with a narrow bandgap of ~0.1 eV and that the $Mo_6S_6$ bundles are metals. Popov et al. further calculated the structural, electronic, and transport properties of bent and twisted $Mo_6S_6$ nanowires by the tight-binding method based on DFT extended with a Green's functions formalism[66]. $Mo_6S_6$ nanowire of 9 nm length with an optimized repeat unit of 4.35 Å was used in the calculations, which showed that bending the $Mo_6S_6$ nanowire by 10° $nm^{-1}$ does not induce plastic deformation in the atomic structure of $Mo_6S_6$ and that the bond length of Mo–Mo changes from 2.70 Å by ±0.08 Å upon bending. These results suggested that $Mo_6S_6$ is a flexible material. However, calculations for a nanowire twisted uniformly by 46° $nm^{-1}$ showed that the Mo triangles do not change and that the bond length between unit cells changes from 2.54 and 2.86 Å. The calculations also revealed that the electronic structure changes more strongly as the twisting angle increases, resulting in plastic working. The increase in the twisting angle changed the band structure of $Mo_6S_6$ from a metal to an insulator with a gap width of ~0.1 eV, and two new VHS were generated at the edge of this bandgap. These results suggest that $Mo_6S_6$ can be used as a conductor or switch in nanodevices.

Zhang et al. used ab initio calculations to show that $M_6X_6$ ($M$ = Cr, Mo, W; $X$ = S, Se, Te) nanowires can be used as efficient catalysts for the oxygen evolution reaction (OER) and oxygen reduction reaction (ORR)[79]. Energy-band calculations indicated that the $Cr_6Te_6$, $Mo_6Te_6$, and $W_6Te_6$ nanowires are semiconductors with narrow bandgaps of 0.45, 0.36, and 0.15 eV, respectively, whereas the other TMC nanowires are metals. A 1×1×2 supercell calculation revealed that the intermediates of the OER and ORR are preferentially bound to metal atoms in the $Cr_6S_6$ and $W_6Te_6$ nanowires, to chalcogen atoms in the $Cr_6Se_6$, $Cr_6Te_6$, and $Mo_6Te_6$ nanowires, and to both atoms in the $Mo_6S_6$, $Mo_6Se_6$, $Mo_6Te_6$, $W_6S_6$, and $W_6Se_6$ nanowires. The active sites of the nanowires differ because of two competing factors that make binding between the intermediates and the nanowires difficult: the chalcogen atoms of the $M_6X_6$ nanowire are over-coordinated, and the metal atoms are located in the center of the nanowire. The results suggest that the $M_6X_6$ nanowires should exhibit excellent catalytic performance.

Jin et al. found that the properties of $M_6X_6$ nanowires ($M$ = Mo,W; $X$ = S, Se, Te) are consistent with the 1D Su–Schrieffer–Heeger (SSH) model, which recognizes 1D topological states from ab initio molecular dynamic simulations[80]. The calculated energy states show that the topological edge states

appeared in the $M_6X_6$ nanowires.

Ying et al. derived the mechanical behavior of $Mo_6S_6$ networks under tensile loading by ab initio calculations and classical molecular dynamics simulations[81]. Their calculations revealed that $Mo_6S_6$ nanowires undergo a phase transformation and that $Mo_6S_6$ hardens when the applied tensile strain is greater than a critical value. Calculation of the engineering strain $\varepsilon$, which is the change in length of a $Mo_6S_6$ nanowire specimen divided by its initial length, also showed that the nanowires elongate without undergoing a structural change at $0 \leq \varepsilon \leq 0.2$ and that their length remains constant in the range $0.2 \leq \varepsilon \leq 0.25$. In addition, $M_6X_6$ nanowires showed a phase transition to the stress-hardening phase as the strain increased in the range $0.25 \leq \varepsilon \leq 0.3$ and a phase transition occurred to the fracture phase at $\varepsilon = 0.3$. These results predict that the results for the tension-induced phase transformation and its effect on the material properties of $Mo_6S_6$ can be extended to other 1D wires such as $Mo_6Te_6$ and $Sn_6Se_6$ nanowires.

Li et al. investigated the stability of $M_6X_6$ ($M$ = Mo, W; $X$ = S, Se, Te) crystals by ab initio calculations for different nanowire arrangements and rotation angles[68]. Their results showed that $M_6X_6$ crystals are most stable when the nanowires are arranged in a rhombic hexagonal type I crystal and when the rotation angle of each nanowire is 15°. The band structure for the hexagonal I array revealed that $M_6X_6$ ($M$ = Mo, W; $X$ = S, Se) crystals are semiconductors with a bandgap less than 0.36 eV, whereas $M_6X_6$ nanowires are metals. Calculations of the occupation of the conduction band also indicated that the nanowires are metallic. From these results, Li et al. concluded that the most stable structure for $M_6X_6$ crystals is a hexagonal I-type array. This finding is consistent with the previously observed structure and electrical transport properties of $M_6X_6$ crystals.

Peng et al. calculated the axial-tensile-strain-induced structural phase transition and changes in the electronic properties of $M_6X_6$ ($M$ = Mo, W; $X$ = S, Se, Te) nanowires using ab initio calculations[82]. Their energy-band calculations showed that $Mo_6S_6$ and $Mo_6Te_6$ nanowires undergo a structural phase transition from stable to metastable structures under applied strain. They also found that, in their stable structures, $Mo_6S_6$ nanowires are metallic and $Mo_6Te_6$ nanowires are semiconducting (bandgap of 0.34 eV), whereas, in their metastable structures, $Mo_6S_6$ and $Mo_6Te_6$ nanowires are both semiconducting (bandgap of 0.62 and 0.80 eV, respectively). Peng et al. further indicated that external tensile strain applied to the $M_6X_6$ nanowires triggered both a structural transition from the stable to the metastable state and an electronic transition from the metallic state to a semiconducting state and an increase in bandgap.

Shang et al. explored the structure and stability of 66 $M_6X_6$ ($M$ = transition metal, $X$ = chalcogen) nanowires by ab initio calculation[83]. They identified 53 experimentally feasible and unprecedented $M_6X_6$ nanowires. Calculations of the Young's modulus for $M_6Te_6$ ($M$ = Cr, Mo, W), $Co_6X_6$ ($X$ = S, Se, Te), and $Fe_6X_6$ ($X$ = S, Se) nanowires with ±2% strain showed that, among the investigated materials, the $Fe_6S_6$ nanowire exhibits the largest Young's modulus (662 GPa). This Young's modulus is

approximately two-thirds that for a single-walled CNT (1000 GPa), which is known as the toughest 1D material. Shang et al. concluded that $M_6X_6$ nanowires are a family of stable 1D vdW interconnect materials with rich physical properties.

Teng et al. used ab initio calculations to study the geometry and electronic band structure of the stable and metastable phases of $Mo_6S_6$ nanowires encapsulated within CNTs[84]. Their DFT calculations revealed that the stable structure of $Mo_6S_6$ nanowires has Mo and S atoms aligned parallel to the nanowires. The optimal chirality index for CNTs was shown to be (16,0) and (9,9) for stable and metastable $Mo_6S_6$ nanowires, respectively. Charge density calculations showed that charge is transferred from the CNTs to the $Mo_6S_6$ nanowires at ~0.14 eV cell$^{-1}$ to ~0.20 eV cell$^{-1}$, indicating strong *p*-type doping in the CNTs. These results are expected to promote the extension of $Mo_6S_6$ nanowires to other 1D TMCs and their practical application in electronic devices.

## 1.3 $MX_3$ and $M_6X_8$

Several groups have investigated TMC crystals such as $MX_3$ and $M_6X_8$. Hoffmann et al. used the extended Hückel method to calculate the bond energies and band structures of the atoms composing $NbSe_3$[85]. Timothy and Hoffmann calculated the band and molecular orbitals of $Mo_{3n}X_{3n+2}$ ($n$ = 2, 3, 4, $\infty$; $X$ = S, Se, Te)[86]. Tarascon et al. also synthesized and measured the physical properties of $AMo_6X_8$ ($A$ = In, Tl; $X$ = S, Se), which they fabricated by diffusing ternary elements into $Mo_6X_8$ at low temperatures[41]. Mu et al. established a method for synthesizing $K_2Mo_3As_3$, which had been difficult to synthesize because of the volatile nature of the constituent elements[87]. $K_2Mo_3As_3$ polycrystalline samples were prepared in two steps via a solid-phase growth method using K pieces, Mo powder, and As powder. First, a mixture of K, Mo, and As elements in an atomic ratio of 2.5:3:3 was heated at 250 °C for 20 h. Next, the heated sample was crushed and pressed into pellets. The pellets were then heated at 850 °C for 50 h. XRD analysis revealed that the space group of $K_2Mo_3As_3$ is *P*-6*m*2, with lattice constants of 10.145 and 4.453 Å in the directions parallel and perpendicular to the needle crystal, respectively.

## 1.4 Purposes

TMCs have attracted attention due to their attractive physical properties derived from 1D quantum confined systems with a three-atom thickness since their discovery in 1980 in bulk crystals of ternary molybdenum chalcogenides[43, 45, 88]. In their isolated and aggregated systems, these nanowires are expected to form electronic systems in 1D, 2D, 3D, and dimensional crossover regions. The development of various preparation methods for these nanowires has to date enabled the fabrication of several and single nanowires from bulk crystals. However, problems such as crystallinity, purity, and size make it difficult to measure the electron transport properties of these samples. To solve this problem, synthesis by CVD method was found to be useful very recently. The CVD method can

synthesize long nanofibers with densely aggregated $W_6Te_6$ nanowires on a substrate with a length of several 10 μm or more. Such nanofibers are expected to have their electronic states and transport properties strongly dependent on their aggregation state. In this study, we have investigated the relationship between the aggregation state and the electronic transport properties of $W_6Te_6$ nanowires.

# Chapter 2

Electron transport properties of WTe nanofiber network

## 2.1 Introduction

TMC nanowires have been reported to exhibit 1D metallic behavior consistent with TLL, rather than the conventional Fermi liquid-like behavior[14, 15, 22]. In addition, nanowires can form various geometries of nanostructures due to vdW interactions between their surfaces. For example, wan atomically thin 2D layer is formed when these nanowires are assembled laterally. Besides this, TMC nanowires can aggregate into 3D bundles. The 1D confinement effect and structural diversity of TMC nanowires have great potential due to their high degree of freedom unlike other functional nanomaterials.

However, studies on TMC nanowires are fairly scarce due to limited samples available. The reason is the lack of viable fabrication methods to produce high quality, long nanowires with high yields. Currently reported synthetic methods include the conversion of similar compounds using lithium-intercalated TMC complexes[14, 15] or 2H-TMDCs[17, 18, 22]. A few studies have reported growth using vapor-phase techniques, such as sulfurization[16], molecular beam epitaxy[24], and nanotemplating reaction inside CNTs[19, 21]. Although these are reliable fabrication techniques, mass production and research of TMC nanowires is challenging due to the small production cost, purity, and sample size.

To solve this issue, we focus our attention on CVD, which is a powerful technique for the largescale synthesis of a diverse range of nanomaterials. Recently, our group has confirmed that the growth substrate affects the structure and morphology of TMC nanowires, and WTe networks consisting of fibrous WTe nanofibers have been observed to be widely and densely distributed on a 25 mm × 30 mm $SiO_2$/Si substrate. In this chapter, we investigate the physical properties of WTe nanofiber network through the electrical conduction and magnetic properties of these samples.

## 2.2 Experimental methods

### 2.2.1 Synthesis of WTe network

WTe nanofiber networks were grown by CVD with temperatures ranging from 700 °C to 800 °C. Specifically, a quartz boat containing anhydrous KBr powder (10 mg, ≥ 99 % purity, Sigma-Aldrich), $WO_3$ powder (100 mg, ≥ 99 % purity, Sigma-Aldrich) and the substrate ($SiO_2$/Si) was first placed in a quartz tube (3 cm in diameter, 100 cm in length) at the center of an electric furnace (ARF-30KC, Asahi-rika Co., Ltd.). An alumina boat with an excess (~2 g) of Te granular (99.99 % purity, Sigma-Aldrich) was positioned upstream at the center of a second identical furnace. After purging the quartz tube with $N_2$ for 15 min, the furnace temperatures were raised simultaneously to 750 °C and 650 °C for the substrate and Te, respectively. The flow of $N_2$ gas was maintained at 582 sccm throughout the experiment. $H_2$ gas was introduced at 18 sccm upon reaching the preset temperatures and maintained

for 5 min. After that, the supply was terminated, and the system was cooled rapidly to room temperature.

### 2.2.2 Characterization

Optical microscopic images were observed with an optical microscope (Nikon, Eclipse-LV100D). A 100× microscope objective (numerical aperture, NA = 0.9) was used to collect a magnified image. Raman spectra of the samples were obtained in a backscattering configuration by using a micro-Raman setup (inVia, Renishaw) at 532 nm (2.33 eV) excitation. A 100× microscope objective same as an optical microscope was used to focus the laser beam and collect scattered light. SEM images were obtained using a desktop SEM (Phenom ProX, Thermo Fisher Scientific Inc.). Topographic images of the WTe nanowires grown on $SiO_2$/Si substrates were acquired in tapping mode over the scan area using a scanning probe microscope (SPM-9600, Shimadzu Corporation). Metal contacts were fabricated on the random network of WTe nanowires grown on $SiO_2$/Si by either depositing conductive silver paste (AXST-50). Electrical and magnetotransport measurements were carried out ina probe station with voltage sources (KEITHLEY, 2614B) and a Quantum Design PPMS system with temperatures ranging from 300 to 1.9 K and a magnetic field up to ±9 T.

## 2.3 Results and discussions

### 2.3.1 Overview of WTe nanofibers network

Figure 2.1 show the SEM images as-grown WTe nanofibers network, respectively. Fiber-like structures are observed to form at high density random network. Different densities of nanofibers were observed at different locations by optical microscope images. Figure 2.2a and b show AFM images of the as-synthesized WTe network taken on in high density and low-density regions, respectively. Figure 2.2c and d show histograms showing height distribution of the aggregated WTe network taken in figure 2.2a and b, respectively. The individual aligned fibers have different sizes, with average thicknesses were 12 nm and 8.5 nm, respectively.

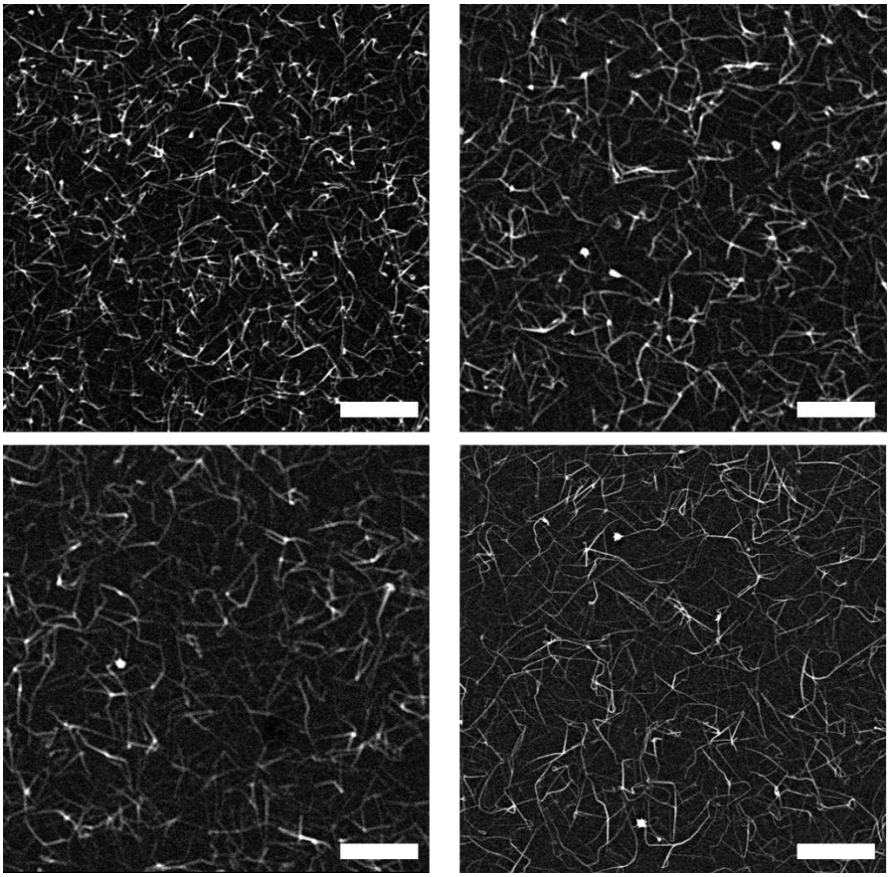

Figure 2.1 SEM image of the as-grown WTe nanofiber network at various locations on $SiO_2$/Si substrate. Scale bars are 10 μm.

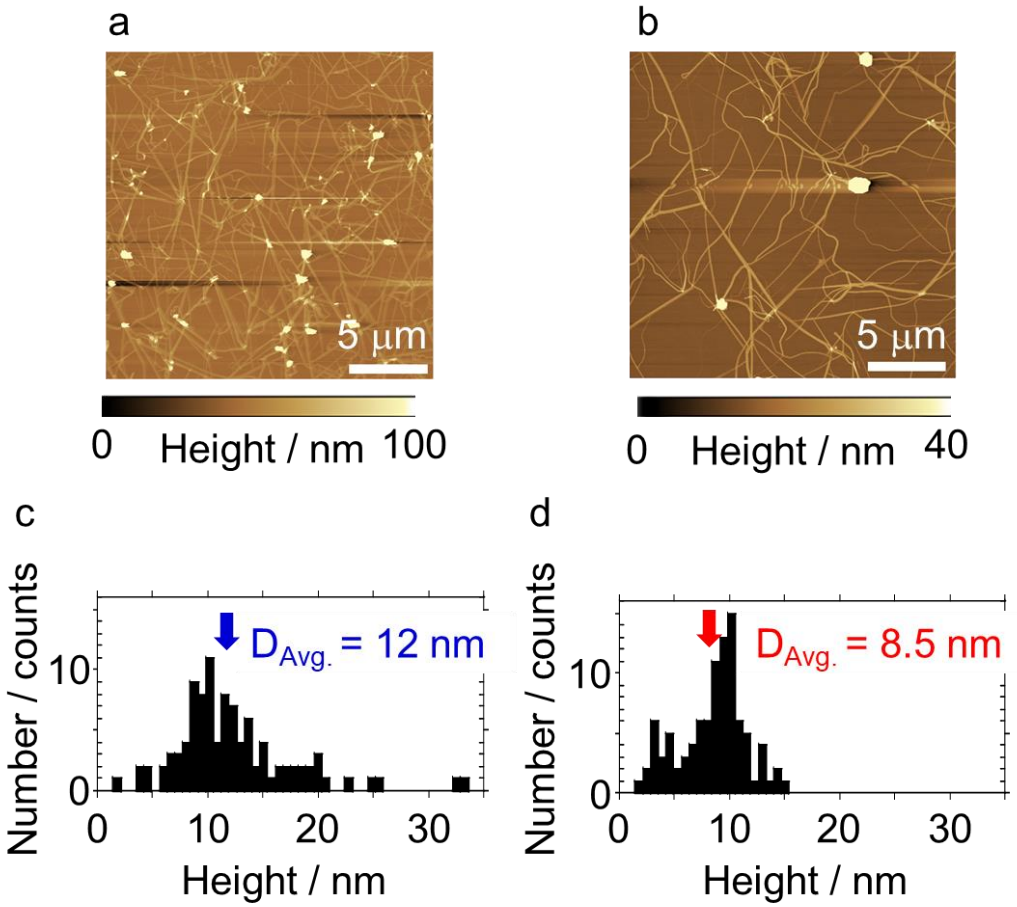


Figure 2.2 AFM image of the as-synthesized WTe network of (a) high and (b) low density. Histograms showing height distribution of the aggregated WTe network taken on (c) figure 2.2a and (d) 2.2b.

## 2.3.2 Electrical transport properties and Magnetoresistance of WTe

The electrical conductivity of the randomly oriented WTe nanofiber networks were monitored using a two-terminal measurement device. Figure 2.3a and b show optical microscope images and I−V characteristic curves of sample 1−4, which the density of nanofibers decreases according to sample 1 to 4. As shown in Figure 2.3b, the voltage drop increases linearly with the current, following an ohmic relationship. Sheet resistance of these samples of Figure 2.3a are estimated to be 11, 97, 2900, and 16000 kΩ/sq, respectively. This result indicates that WTe networks with higher nanofiber density have lower sheet resistance. Such low sheet resistance is likely due to the relatively low inter bundle contact resistance, suggesting the potential application of WTe nanowires as transparent, flexible, and conductive films. Figure 2.4a and b show the temperature dependence of the conductance and conductance normalized by the values of 300K as a function of the temperature of WTe networks respectively. As the temperature is lowered, the conductance increases for samples with conductance above 1 μS at 300 K, while the conductance decreases for samples with conductance below 1 μS.

Conductance increases with decreasing temperature for samples with conductance above 1 μS at 300 K. On the other hand, for samples with conductance below 1 S at 300 K, conductance decreases with decreasing temperature, and the conductance is proportional to a power of temperature up to 100 K. This result suggests that the WTe nanofiber network may constitute a TLL. The metallic behavior of the WTe nanofiber network is confirmed by the temperature dependence of the electrical resistance. In Figure 2.5a, a monotonic decrease in resistance is observed as the temperature decreases from 300 to 10 K. The increase in resistance below 10 K is likely due to the electron localization effect in low-dimensional systems. This temperature dependence exhibits a higher residual resistivity ratio than previously reported MoTe networks, as well as remarkable metallic properties[73]. Figure 2.5b and c shows the magnetoresistance (MR) of these conductive WTe networks plotted as a function of $B^2$ at various temperatures. Here, MR is defined as $[\rho(B) - \rho(0)]/\rho(0)$, where $\rho(0)$ and $\rho(B)$ refer to the resistivity in a zero and an applied magnetic field $B$, respectively. The MR increases with increasing magnetic field. The linear dependence of MR with $B^2$ observed from 60 to 40 K indicates classical metallic behavior subject to Lorentz forces. In contrast, a nonlinear $B^2$ dependence is observed below 30 K. Considering the electrical resistance curve in Figure 2.5a, the cusp-like positive MR that appears at low temperature can be attributed to the weak antilocalization (WAL) effect originating from the spin−orbit interaction, which usually predominates as material thickness decreases[89]. However, the cause of WAL has not been identified. To solve these problems, it is necessary to synthesize single WTe nanofibers and investigate their electron transport properties.

## 2.4 Conclusion

In conclusion, we observed that the density of nanofibers in the WTe nanofiber network differs depending on the location and that the nanofibers in the network are thicker when the density is larger. The electrical transport properties of the samples with large conductance were found to be metallic, while those with small conductance showed a decrease in conductance with a power of temperature. In comparison with similar studies of $Li_2Mo_6Se_6$ nanofibers[15], these data suggest that $W_6Te_6$ nanofibers also exhibit electron transport properties that reflect the size of the nanofibers

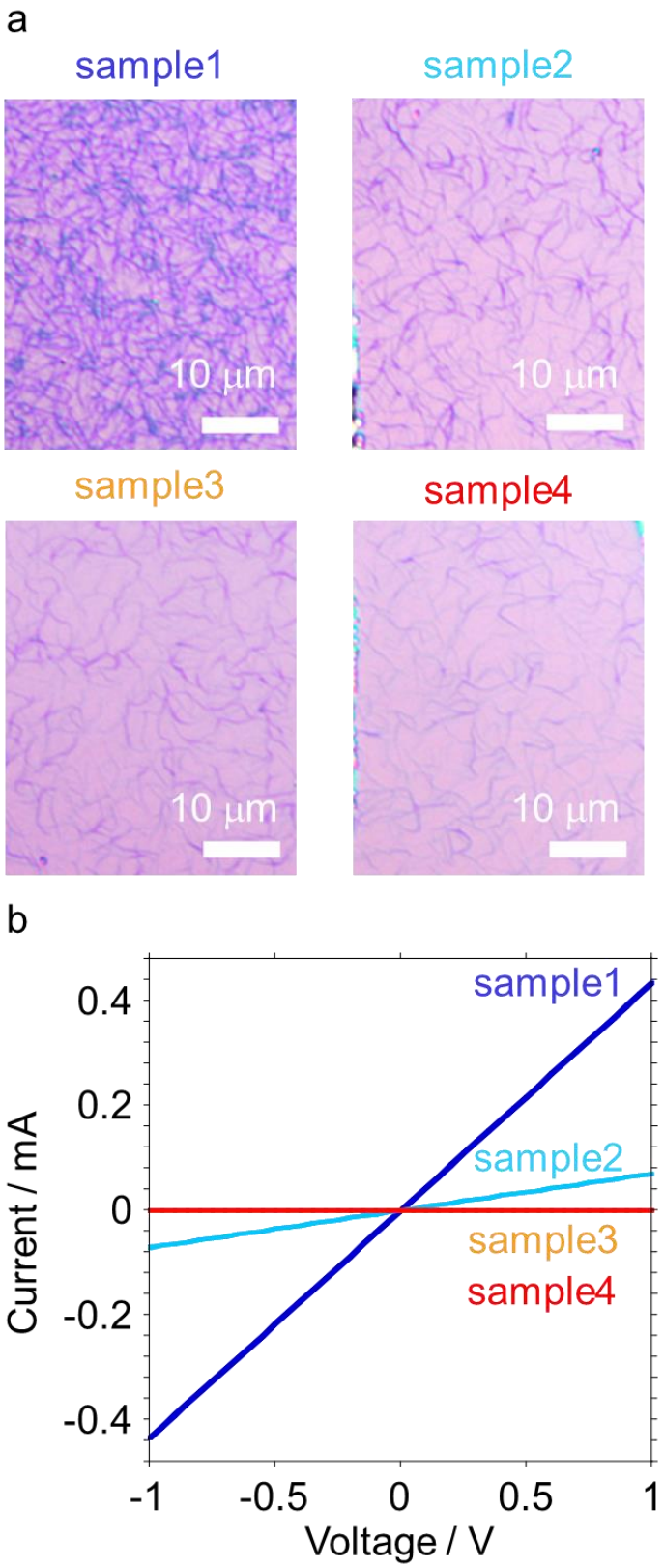


Figure 2.3 (a)Optical microscope images and (b) I−V characteristic curves for a WTe thin film grown on a $SiO_2$/Si substrate measured at room temperature indicated in Figure 2.3a.

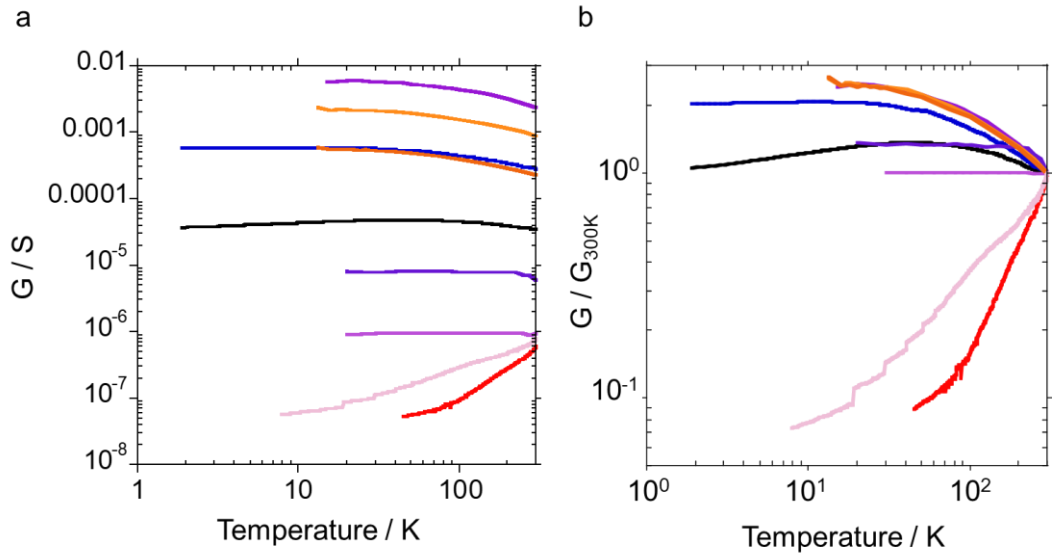


Figure 2.4 The temperature dependence of (a) the conductance and (b) conductance normalized by the conductance of 300 K of WTe networks

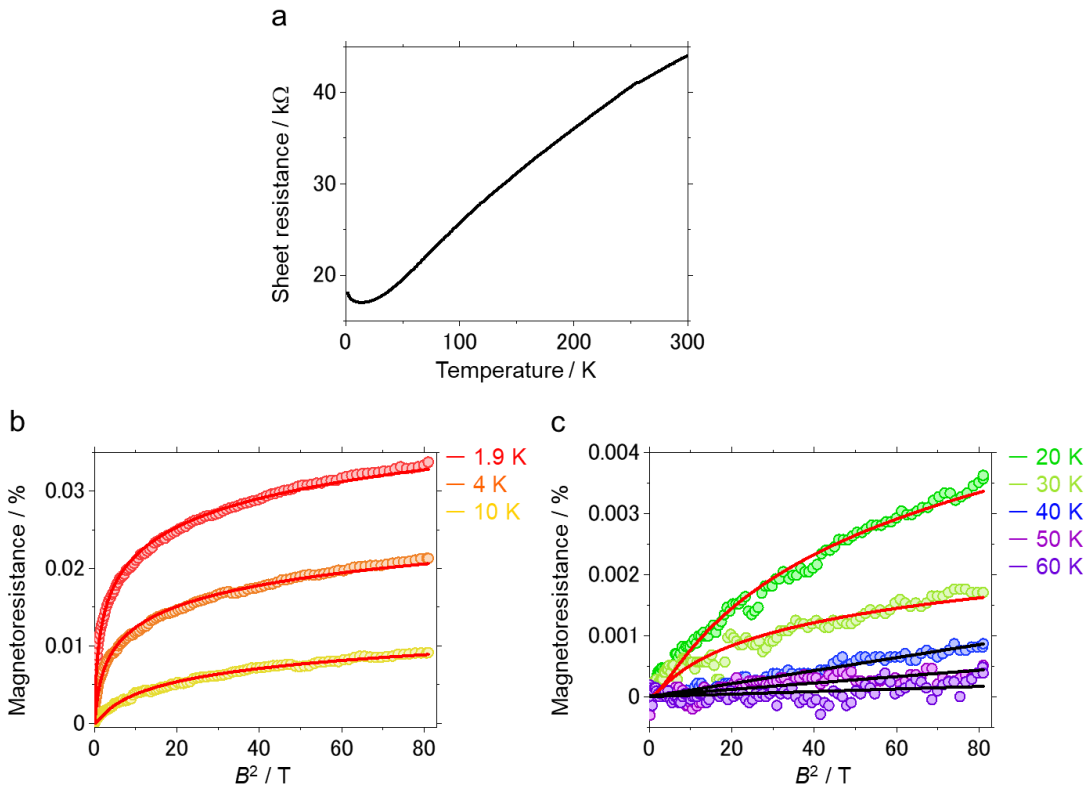


Figure 2.5 (a)Temperature dependence of the electrical resistance of the WTe nanofiber network. Magnetoresistance as a function of $B^2$ of (b)1.9 ~ 10 K and (c) 20 ~ 60 K. Solid curves correspond to linear (black) and power law (red) fits.

# Chapter 3

Formation of a two-dimensional electronic system in laterally assembled WTe nanowires

## 3.1 Introduction

A single TMC wire is composed of vertically stacked units of $M_6X_6$ triangles, where $M$ and $X$ represent transition metal and chalcogen atoms, respectively, along the wire axis, and the individual wires form aggregates through vdW interactions (Figure 3.1a, b). The electronic properties of TMC wires can possibly be tuned by manipulating the assembled crystal structure. Metal−semiconductor transitions have been reported for single to a few wires of WTe grown by molecular beam epitaxy[20]. For example, a single wire is a narrow-band gap semiconductor, while bundles of a few wires become a metal. In contrast to a single 1D TMC wire, we recently achieved wafer-scale production of atomically thin layered and bundled aggregates of WTe and MoTe nanowires by CVD, which has provided aggregates of various structures, such as 2D layers and 3D bundles[23]. This work also reveals that WTe bundles show metallic properties based on transport measurements and calculated band structures. These aggregates could provide an ideal platform to create wire-based 1D, 2D, 3D, and their cross-over systems such that a series of transport properties could be expected, depending on their dimensionality. However, in our previous study, intentional aggregation of 1D TMCs as building blocks into isolated 2D-layered materials was still difficult because the samples were typically networks of high-density WTe bundles. To solve this issue, improvements in the CVD growth process are highly desirable to prepare sufficiently long, isolated TMC 2D bundles. Here, we report an improved CVD growth process that realizes single bundles of laterally assembled WTe nanowires, resulting in the observation of quantum oscillations derived from a 2D carrier gas. The long, isolated ribbon-shaped WTe bundles can be grown by high-temperature CVD. The morphology and atomic structure of the samples were characterized by atomic force microscopy (AFM) and high-angle annular dark-field scanning transmission electron microscopy (HAADF-STEM). In addition, magnetoresistance (MR) measurements were conducted to investigate the transport properties of single WTe bundles.

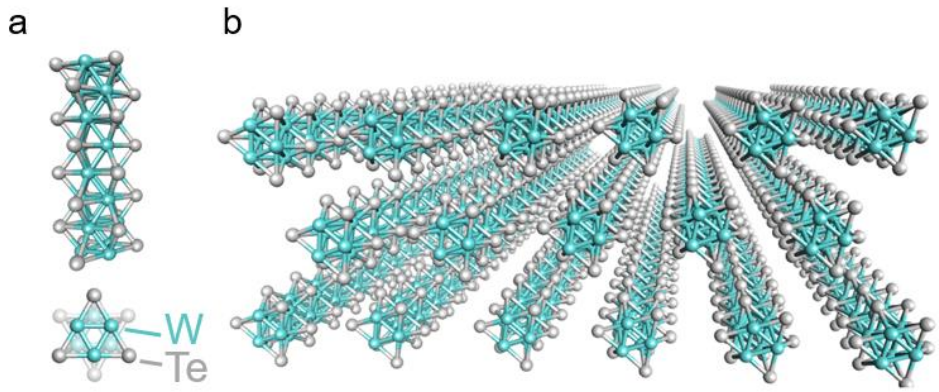


Figure 3.1 Schematic diagrams of (a) a WTe nanowire composed of staggered $W_3Te_3$ triangular units and (b) a 2D aggregate formed from 1D WTe wires. Blue and gray spheres correspond to W and Te atoms.

## 3.2 Experimental methods

### 3.2.1 WTe Synthesis

WTe atomic wires were grown using an in-house built CVD system with two electric furnaces (ARF-30KC, Asahi-rika Co., Ltd.), as shown in Figure 1c. A quartz boat containing anhydrous KBr powder (100 mg, ≥ 99%, Sigma–Aldrich), WO3 powder (200 mg, ≥ 99%, Sigma–Aldrich) and the substrate ($SiO_2$/Si) was first placed in a quartz tube (3 cm diameter, 100 cm length) at the center of the downstream furnace. An alumina boat with an excess (ca. 3 g) of granular Te (99.99%, Sigma–Aldrich) was positioned at the center of the upstream furnace. After purging the quartz tube with $N_2$ for 10 min, the furnace temperatures were simultaneously raised to 890 °C and 700 °C for the substrate and Te, respectively. The flow of $N_2$ gas was maintained at 291 sccm throughout the experiment. $H_2$ gas was introduced at 9 sccm upon reaching the preset temperatures and maintained for 5 min. The system was then rapidly cooled to room temperature.

### 3.2.2 Characterizations

SEM images were obtained using a desktop SEM system (Phenom ProX, Thermo Fisher Scientific Inc.). For STEM, HAADF images were taken at room temperature using a cold field emission gun (JEM-ARM200F, ACCELARM) operated at 120 kV and equipped with a CEOS ASCOR corrector. Ten HAADF-STEM images were summed after drift compensation, with each image having a dwell time of 3 μs per pixel. EDS elemental analysis (JED-2300, JEOL) was also performed. Cross-sectional samples were prepared using focused ion beam milling. Topographic images of WTe atomic wires grown on $SiO_2$/Si substrates were acquired in noncontact mode using a scanning probe microscope (NX10, Park Systems). Raman spectra of WTe bundles were measured by using a Raman microscope (inVia, Renishaw) with an excitation laser operating at 532 nm excitation. (IV) Device fabrication and

transport measurements. Metal contacts were fabricated on WTe bundles grown on $SiO_2$/Si by deposition of In/Au (5 nm/20 nm) using a thermal evaporator. Electrical and magnetotransport measurements were performed in a physical property measurement system (PPMS, Quantum Design) with the temperature ranging from 300 to 1.9 K and a magnetic field of up to ±9 T. Transport measurements down to 0.77 K were conducted using a cryostat combined with a helium-3 gas handling system and an AC resistance bridge (Lakeshore 370).

### 3.2.3 Device fabrication and transport measurements

The electronic structure of a WTe bundle was investigated using DFT[90, 91] implemented in the STATE program package[92, 93]. The exchange-correlation potential energy among interacting electrons was treated by the generalized gradient approximation with the Perdew-Burke-Ernzerhof functional[94]. Ultrasoft pseudopotentials were adopted to describe the interactions between electrons and nuclei[95]. The valence wave function and deficit charge density in the core region were expanded in terms of plane wave basis sets with cutoff energies of 25 $R_y$ and 225 $R_y$, respectively. Integration over the Brillouin zone was conducted using equidistant 2×4×8 k-meshes, which were used for the self-consistent electronic structure calculations. The atomic coordinates of the WTe wires were optimized until the force acting on each atom became less than 5 mRy $Å^{-2}$ under the experimentally obtained lattice parameters. Electronic eigenvalues were calculated using 41 × 71 k-meshes to draw the Fermi surfaces on the $k_y$-$k_z$ plane.

## 3.3 Results and discussions

### 3.3.1 Synthesis and Crystal orientation of WTe

WTe bundles were grown on $SiO_2$/Si substrates by CVD, as previously reported (Figure 3.2a)[23]. The growth temperature was set to 890 °C to obtain low-density and long bundles. Compared to growth at 750 °C (Figure 3.2b), the high temperature effectively suppresses the nucleation density and encourages WTe elongation (Figure 3.2c−e). There is little difference in the Raman spectra at different growth temperatures (Figure 3.2f). This means that the crystallinity of the wires is maintained even under the present high-temperature growth conditions. A typical bundle with a length of more than 100 μm is shown in the inset of Figure 3.2c. The difference can be explained by the Ostwald ripening of the nucleation droplets, which occurs at an elevated temperature. During WTe growth, precursors can react and form intermediate droplets that deposit on the substrate surface[23]. These smaller size droplets tend to combine into energetically advantageous, larger islands with a smaller surface area per unit volume as the temperature increases. The nucleation density across the substrate is thus reduced, while the larger seeds promote the continuous growth of WTe with a greater supply of reactants. When the reaction temperature is increased, long and low-density WTe bundles are grown as a result. The present WTe bundles also have a thin, anisotropic structure with a width of 130−280

nm and a thickness of 6−30 nm, according to AFM observations (Figure 3.3a, b). This allows for almost isolated ribbon-shaped aggregates to be built up from 1D WTe wires, which enables the fabrication of a two-terminal device on a single WTe bundle by conventional photolithography.

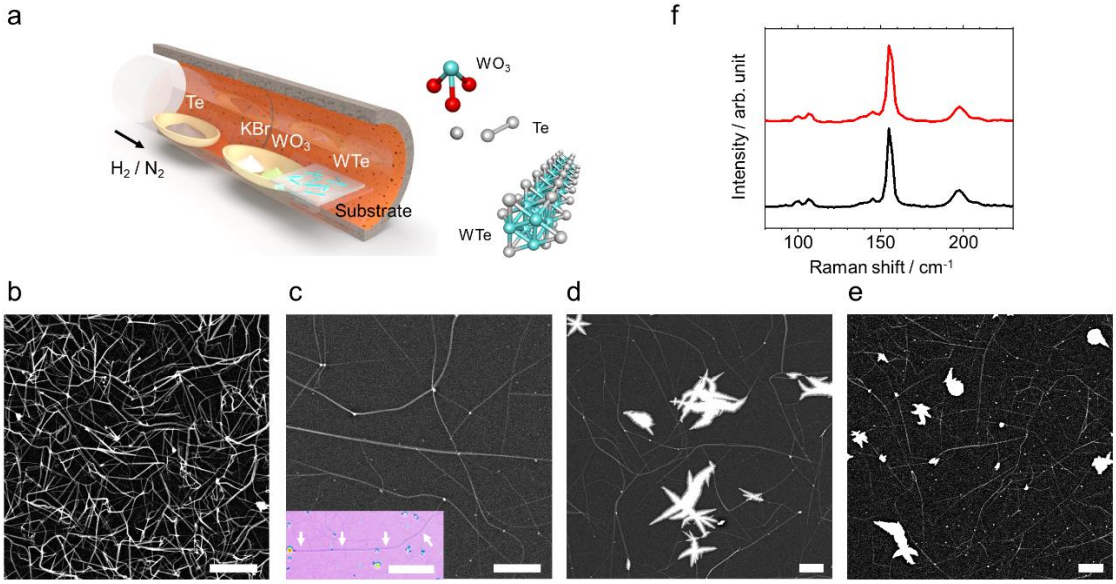


Figure 3.2 (a) Schematic illustration of the setup used for the synthesis of bundles and growth of WTe nanowires from $WO_3$ and Te precursors. Growth was conducted via vapor-phase evaporation of solid precursors with the aid of an alkali metal salt as a growth promoter. Plan-view SEM image of (b) a network of WTe bundles (synthesized at 750 °C) and (c−e) isolated long WTe bundles (synthesized at 890 °C). Scale bars are 5 µm. The inset in (c) shows an optical microscope image of a single WTe bundle longer than 100 µm. Scale bar is 50 µm. (f) Raman spectra of WTe bundles grown at (black) 750 °C and (red) 890 °C.

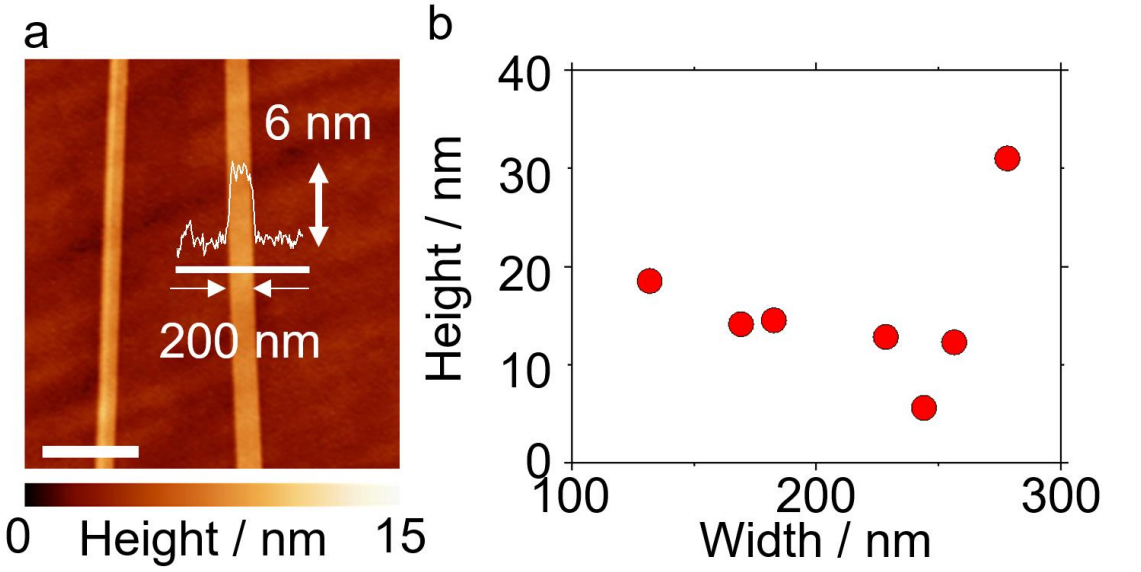


Figure 3.3 (a) AFM topographic image of WTe bundles. The height profile was obtained along the white line. Scale bar is 1 μm. (b) Plot of the height and width of individual WTe bundles.

The atomic structure of a WTe bundle was observed using cross-sectional HAADF-STEM, as shown in Figures 3.4a, b, and c. Figure 3.4a shows that the bundle has a thickness of 12 nm and can be regarded as a single crystal composed of aligned individual wires. Thinner ribbon-shaped aggregates (~4 nm thickness) of WTe wires are also shown in Figure 3.4b. Figure 3.4c shows that the WTe bundle has a simple monoclinic lattice, as previously reported[23]. The distance between the neighboring wires is 0.89−0.91 nm. The unit cell of a WTe crystal contains two wires, as shown in Figure 3.4d, and the lattice constant in the wire axial direction, c, is 4.45 nm[23] because there is a c/2 shift along the wire axial direction between the neighboring wires. From a comparison with the crystal structure of MoTe wires[18], the lattice constants of the present WTe crystals were estimated to be 0.91 and 1.79 nm for the [010] and [100] directions, respectively, with an angle of 58°. One side of the $W_3Te_3$ triangular units is rotated 9° from the [100] axis. These lattice parameters for WTe crystals are almost the same as those for MoTe crystals[18]. Figure 3.5a−c shows a wide-view cross-sectional STEM image and the corresponding energy dispersive X-ray spectroscopy (EDS) elemental mapping. These images reveal that the bundle has a width of 100 nm and consists of W and Te, as confirmed by the EDS spectrum (Figure 3.5 d), verifying the construction of ribbon-shaped materials from 1D WTe wires.

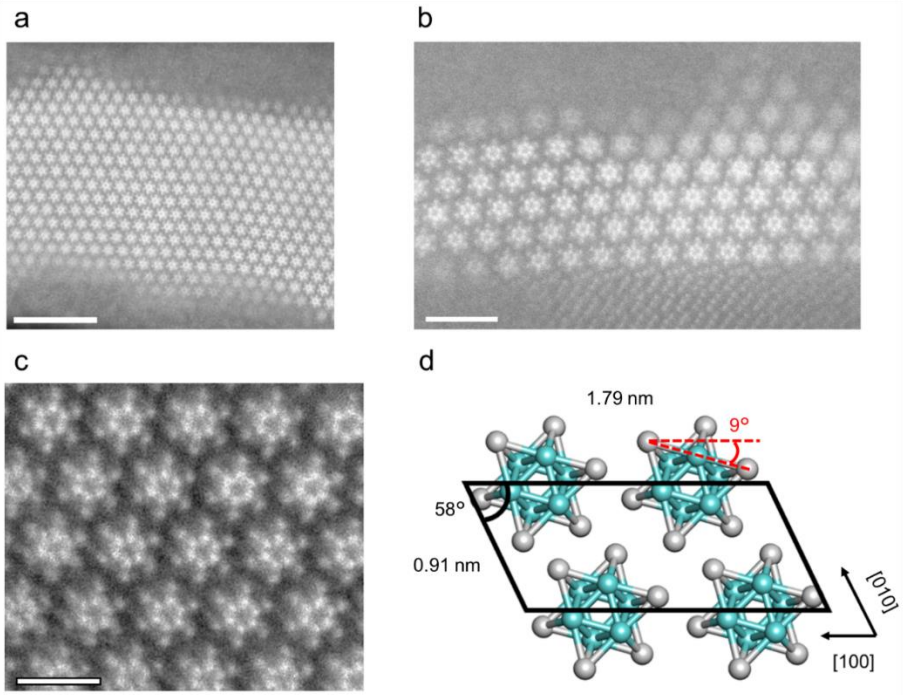


Figure 3.4 (a–c) Cross-sectional HAADF-STEM images of an as-grown WTe bundle captured under different magnifications. The bundle consists of well-aligned WTe subunits stacked into a thin layer. Scale bars are 5 nm in (a), 2 nm in (b), and 1 nm in (c). (d) Schematic diagram of the unit cell of a WTe bundle

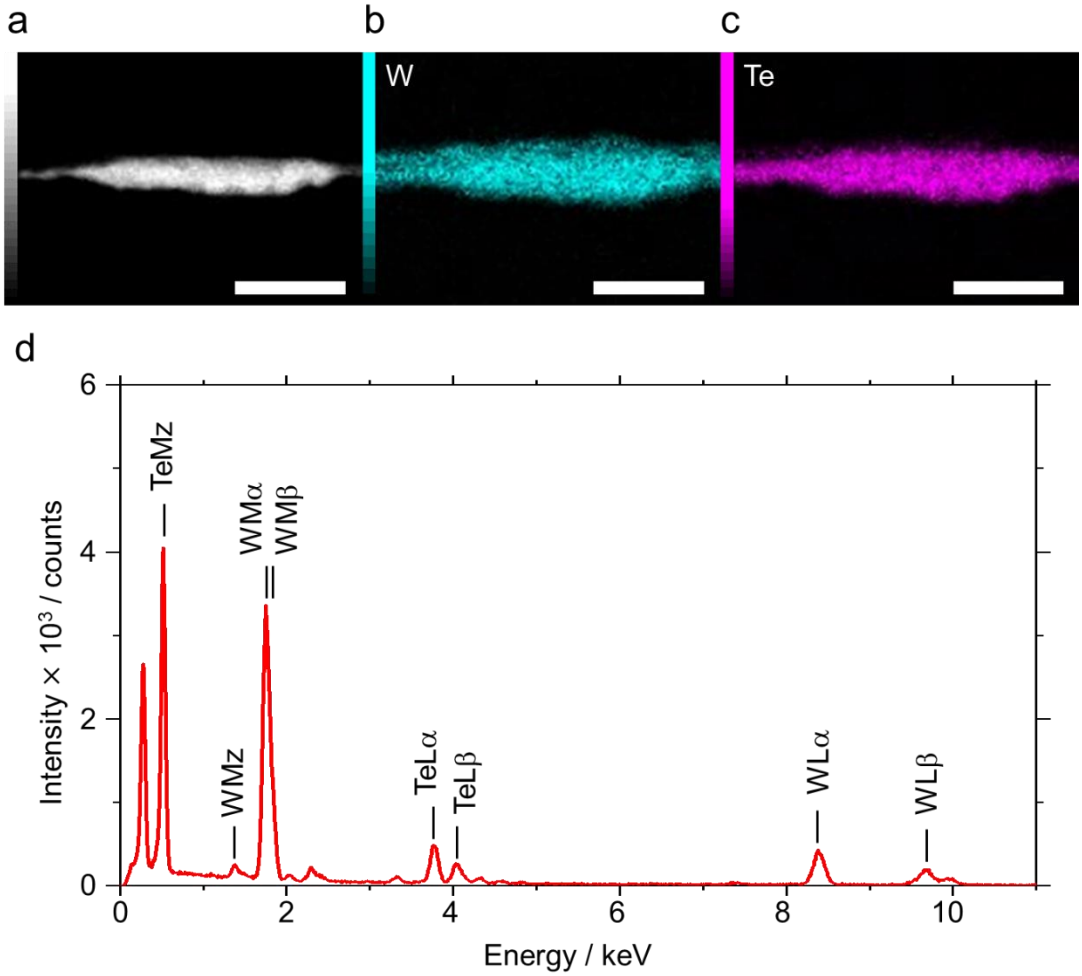


Figure 3.5 (a) Low-magnification HAADF-STEM image of a WTe bundle, and (b and c) corresponding EDS elemental maps of W and Te. Scale bars are 50 nm in (a), (b), and (c). (d) EDS spectrum of a WTe bundle.

### 3.3.2 Electron transport properties and magnetoresistance effect of WTe

To characterize the transport properties of WTe, the magnetotransport in a single bundle of WTe nanowires was measured using In/Au electrodes (Figure 3.6a, c, and e). AFM images of three samples (samples 1−3) are presented in Figures 3.6b, d, and f. These WTe bundles exhibit metallic behavior, where the resistance decreases with a decrease in temperature between 5 and 300 K, whereas at low temperatures below 5 K, the resistance increases with a decrease in temperature (Figures 3.7a), similar to the previously reported WTe random network[23]. Moreover, superconductivity was not observed down to 0.77 K (Figure 3.7b). Because the resistance increase at the lowest temperature was previously assigned to the weak antilocalization (WAL) effect[23], magnetoresistances (MR) measurements were also performed for isolated WTe bundles. WAL is usually observed in low-dimensional systems with heavy atoms at low temperatures. In this situation, the quantum interference of spin-flipped back-scattered electrons is enhanced. Applying a magnetic field to the WAL system increases the probability of backscattering by suppressing the interference effects, thus increasing resistivity. A magnetic field of up to 9 T was applied perpendicular to the substrate, and the MR was calculated as $[R(B) - R(0)]/R(0)$, where $R(B)$ is the resistance when magnetic field $B$ is applied. Figure 3.8a shows that the single WTe bundle exhibits distinct magnetic-field-dependent oscillations and an increase in the MR. As reported in our previous study[23], the monotonically increasing MR component with a magnetic field could be explained by the WAL effect; however, the oscillation behavior has not been observed. This effect is only observed in high-quality ribbon-shaped bundles; therefore, such oscillation behavior suggests 2D Shubnikov-de Haas (SdH) oscillations because of the 2D distribution of a carrier gas. SdH oscillation is a phenomenon in which the resistance oscillates when a magnetic field is applied to metal. This oscillation is caused by Landau quantization, which is the quantization of the energy levels of an electron in a magnetic field. Due to Landau quantization, increasing the magnetic field leads to changes in the density of states, resulting in the oscillation of resistivity. This phenomenon is mainly observed in high-quality single crystals. In the following, we will analyze the oscillation components and the monotonic increase in the MR curves.

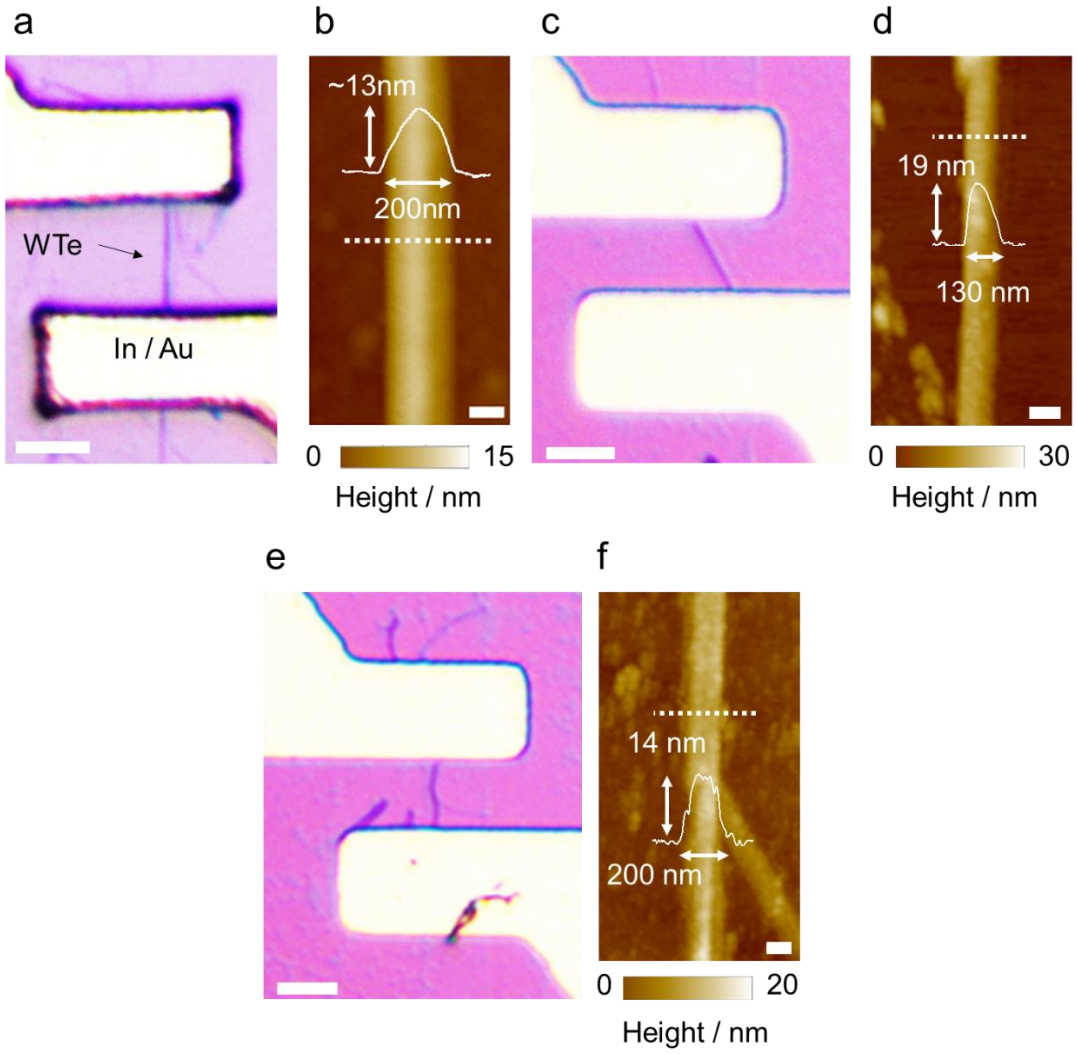


Figure 3.6 Optical microscopy and AFM images for an isolated WTe bundle of (a, b) sample 1, (c, d) sample 2, and (e, f) sample 3. The height profiles were obtained along the white dotted lines. Scale bars are 5 μm in (a, c, e) and 100 nm in (b, d, f).

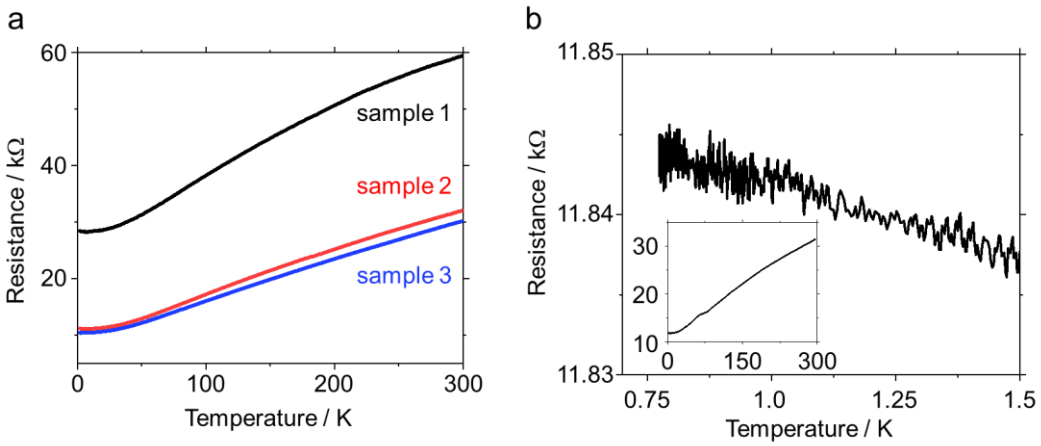


Figure 3.7 (a) Temperature dependence of the electrical resistance for samples 1−3, as shown in Figure 3.6 a−f. (b) Temperature dependence of the electrical resistance down to 0.77 K. The inset shows the temperature dependence of the electrical resistance from 300 K to 0.77 K.

The relationship between the MR and the magnetic field angle was measured to investigate the possibility of SdH oscillations because of a 2D carrier gas. Figure 3.8a presents $R(B)$ measured at $T$ = 1.9 K for different angles θ. The inset of Figure 3.8a shows that at $\theta = 0°$, the magnetic field is applied perpendicular to the substrate surface, while at $\theta = 90°$, the magnetic field is applied parallel to the substrate surface and perpendicular to the wire axial direction. The oscillation peaks shift to a higher magnetic field as $\theta$ increases. To clearly capture these changes, the derivatives of the magnetic field curves as a function of $B^{-1}$ and $(B \cos \theta)^{-1}$ are shown in Figure 3.8b, c, respectively. Notably, the oscillation depends on the perpendicular component, $(B \cos \theta)^{-1}$, of the magnetic field. These results strongly indicate that the oscillation is derived from the cyclotron motion of a 2D carrier gas formed in the WTe bundle.

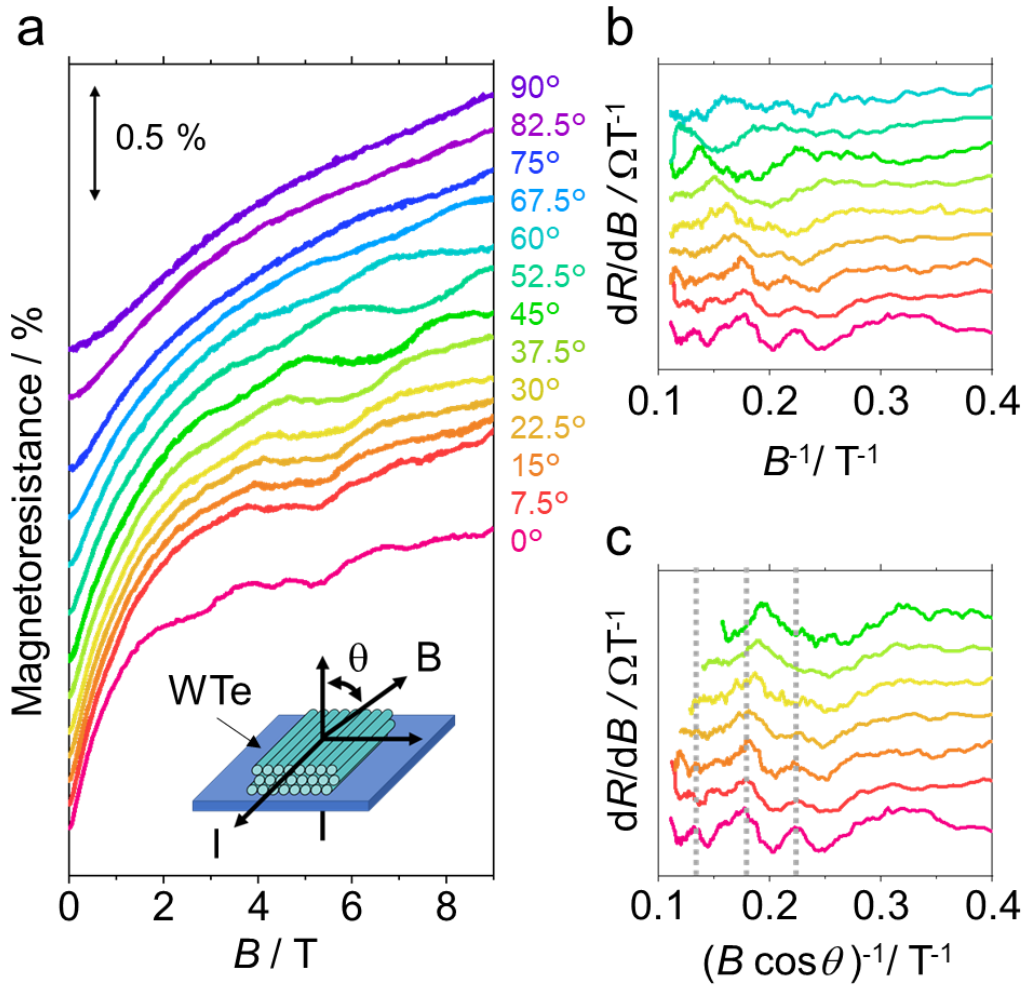


Figure 3.8 (a) MR as a function of magnetic field $B$, recorded at different orientations (measured by the angle $\theta$) with respect to the substrate normal. (b) Numerical derivative d$R$/d$B$ as a function of $B^{-1}$, the inverse of the magnetic field component perpendicular to the sample. (c) d$R$/d$B$ as a function of $(B \cos \theta)^{-1}$. An offset was introduced into each curve for clarity. Gray dotted lines are given as a guide.

Several physical parameters were derived based on the SdH oscillations of the 2D carrier gas. The carrier density $n$ and mobility $\mu$ can be estimated using the relationships $n = ef/\pi\hbar$ and $\mu = L/enRW$, where $e$ is the elementary charge, $f$ is the oscillation frequency, $L$ and $W$ are the length and width of the WTe bundle between the electrodes, respectively, and $R$ is the electrical resistance. The frequency was estimated to be 20 T (an oscillation period of 0.05 $T^{-1}$) from the prominent peaks below 0.25 $T^{-1}$, as shown in Figure 3.8c, which are less affected by localization effects. This leads to a carrier density of $9.7 \times 10^{11}$ $cm^{-2}$. Assuming that this is the total carrier density, the mobility is estimated to be 8400 $cm^2$ $V^{-1}$ $s^{-1}$. However, the contribution of other Fermi surfaces must be considered because a 3D crystal and a 2D layer of WTe wires are predicted to be a semimetal with multiple electron and hole bands from density functional theory (DFT) calculations[23]. To clarify the contribution from other bands, further studies involving MR measurements in higher magnetic fields are required in the future. In this work, the type of majority carrier was determined to be holes from the sign of the Seebeck coefficient at room temperature (Figure 3.9)[23]. Although there is a possibility of overestimation, the estimated mobility of the WTe bundle is higher than that of semimetal $WTe_2$ flakes with a similar thickness of 13 nm (1000−2000 $cm^2$ $V^{-1}$ $s^{-1}$ for holes and electrons at 1.8 K) and is comparable to that of WTe flakes with a thickness of 150 nm (4000 $cm^2$ $V^{-1}$ $s^{-1}$ for holes and 7000 $cm^2$ $V^{-1}$ $s^{-1}$ for electrons)[96]. This suggests the potential for future application of WTe bundles as electronic materials.

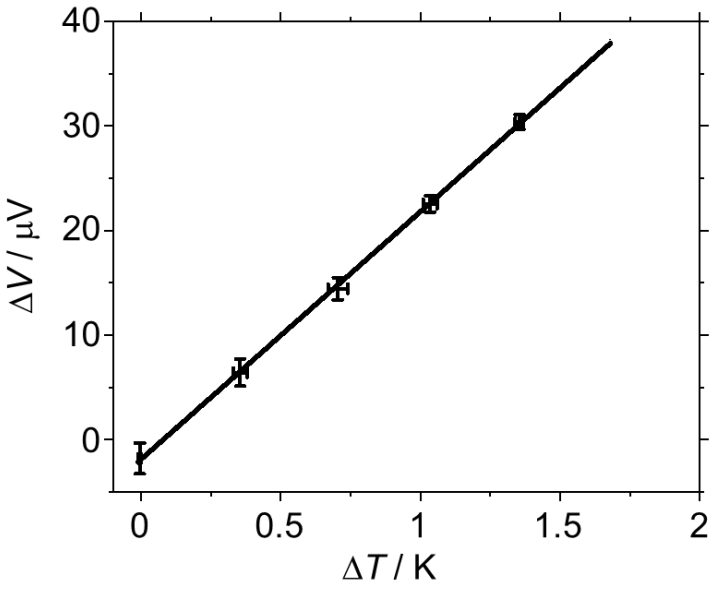


Figure 3.9 Seebeck coefficient for a WTe network. $\Delta T$ dependence of the electric voltage difference $\Delta V$ (open circles) for a network of WTe bundles at 300 K. The solid line indicates a linear approximation.

The present 2D carrier gas was further characterized by the temperature change of the MR, which enabled analysis of the cyclotron mass, $m^*$. Figure 3.10a presents the MR for a WTe bundle measured from 1.9 to 8 K. A magnetic field of up to 9 T was applied perpendicular to the substrate. At 8 K, the MR monotonically increased when a magnetic field was applied, and this behavior tended to be more pronounced at lower temperatures, as observed for the networks of WTe bundles. To analyze the data, the oscillation components $\Delta R_{SdH}$ in the high magnetic field region (3 T) were extracted by subtracting the linear background component due to the WAL effect (Figure 3.10b). Figure 3.10c shows $\Delta R_{SdH}$ at the oscillation peaks plotted as a function of temperature for different magnetic fields. $|\Delta R_{SdH}|$ can be well reproduced by the following equation:

$$\Delta R \propto \frac{2\pi^2 m^* k_B T/\hbar eB}{\sinh(2\pi^2 m^* k_B T/\hbar eB)},$$

where $k_B$ is the Boltzmann constant, and the cyclotron mass $m^*$ can be determined from the $\Delta R_{SdH}$ curve fitting. The ratio of $m^*$ to the free electron mass me is 0.2 on average according to the data at six different magnetic fields. This value is relatively small compared with layered transition metal dichalcogenides (TMDCs), such as few-layer $MoS_2$ ($m^*/m_e$ = 0.27±0.01) and $WS_2$ ($m^*/m_e$ = 0.20±0.04)[97] and mono- and bilayer $WSe_2$ ($m^*/m_e$ = 0.45)[98]. The cyclotron radius $r$ is roughly estimated using the relationship from classical mechanics, $r = m^* v_F/eB$, where $v_F = \sqrt{2e\hbar f}/m^*$ is the Fermi velocity for the 2D carrier gas. r was roughly estimated to be 37 nm at 4.4 T using a $v_F$ of 172 km $s^{-1}$ at 1.9 K, which is significantly smaller than the sample width of 200 nm.

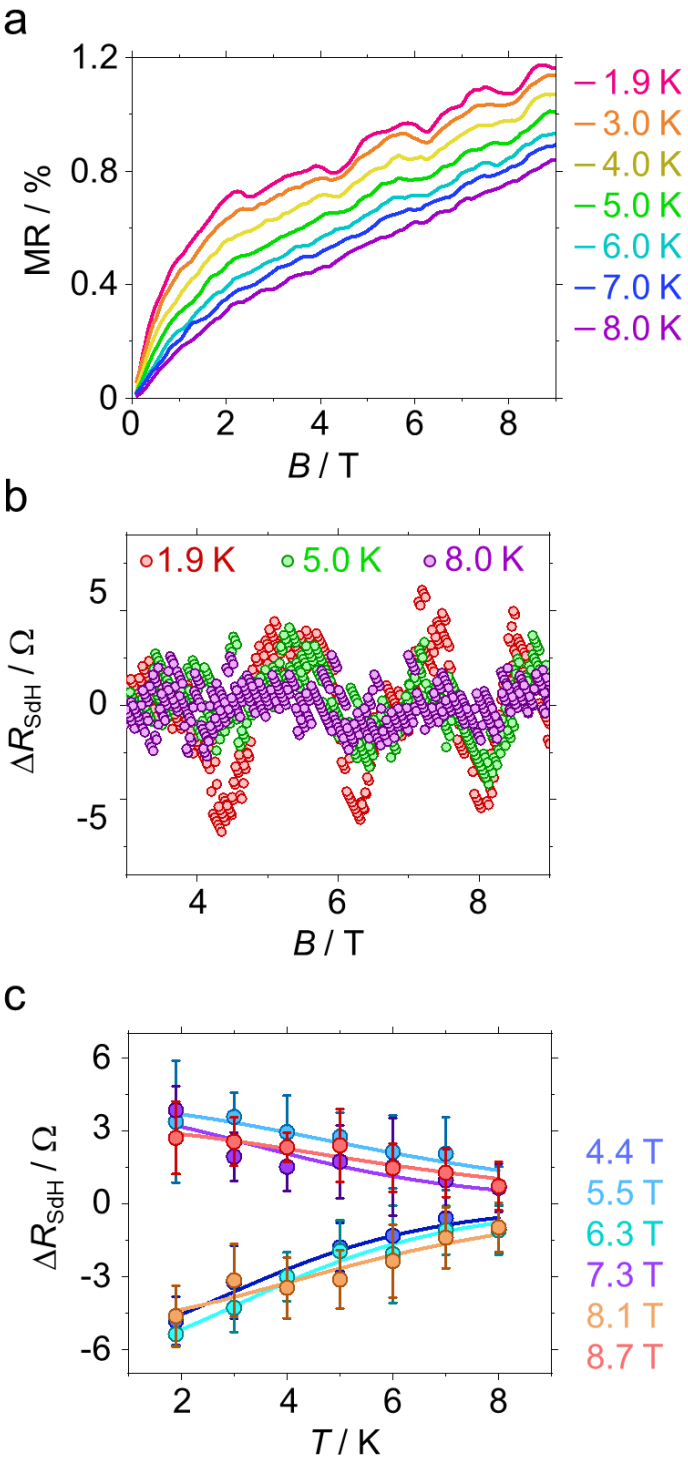


Figure 3.10 (a) MR plotted as a function of applied magnetic field $B$ oriented perpendicular to the substrate, recorded at different temperatures $T$. (b) MR obtained by subtracting the linear background from (a) at 1.9, 5.0, and 8.0 K. (c) Oscillation components $\Delta R_{SdH}$ at the oscillation peaks plotted as a function of temperature for different magnetic fields.

The monotonic increase in the MR component with magnetic field is explained by the WAL effect. Here, the dimensionality of the electronic transport properties was also investigated with respect to the WAL effect. As shown in Figure 3.11a and b, the magnetoconductance (MC) $\Delta\sigma$ curves can be well reproduced by the sum of the classic MC, $\Delta\sigma(B) \propto B^2$, and the Hikami–Larkin–Nagaoka theory for WAL[99]:

$$\Delta\sigma(B) = \sigma(B) - \sigma(0) = -\frac{e^2}{2\pi^2\hbar}\left[\frac{1}{2}\Psi\left(\frac{1}{2}+\frac{B_\phi}{B}\right) - \frac{1}{2}\ln\left(\frac{B_\phi}{B}\right) - \Psi\left(\frac{1}{2}+\frac{B_\phi+B_{SO}}{B}\right) + \ln\left(\frac{B_\phi+B_{SO}}{B}\right) - \frac{1}{2}\Psi\left(\frac{1}{2}+\frac{B_\phi+2B_{SO}}{B}\right) + \frac{1}{2}\ln\left(\frac{B_\phi+2B_{SO}}{B}\right)\right],$$

where $\hbar$ is the Dirac constant, $\Psi$ is the digamma function, $B\phi=\hbar/4eD\tau\phi$ is determined by the electron phase coherence time $\tau\phi$, and the diffusion constant $D$, and $Bso=\hbar/4eD\tau_{SO}$ is determined by the spin relaxation time $\tau_{SO}$ and $D$. The phase coherence length $L\phi$ and the spin-orbit scattering length $L_{SO}$ are also estimated using the relationships $L\phi=\sqrt{D\tau_\phi}=\sqrt{\hbar/4eB_\phi}$ and $L_{SO}=\sqrt{D\tau_{SO}}=\sqrt{\hbar/4eB_{SO}}$, respectively. $B\phi$, $B_{SO}$, $L\phi$ and $L_{SO}$ are plotted as a function of temperature (Figures 3.11c and d). The increase in $L\phi$ is consistent with the temperature dependence of the resistance due to WAL, while $L$so has a weak temperature dependence. $L\phi$ increases with decreasing temperature and reaches approximately 70 nm at 1.9 K. The relationship between $L\phi$ ($B\phi$) and temperature $T$ can be approximated as $L\phi \propto T^{-0.5}$ ($B\phi \propto T$), which is consistent with the theoretically predicted dephasing mechanism that includes electron-electron interactions in the 2D WAL effect[100], and a similar behavior is also observed for other 2D electron systems[67, 101-103]. The present WTe system shows both 2D WAL and SdH oscillations of a 2D gas. This could be explained by the different contributions of surface and bulk carriers. The 2D WAL is probably due to the surface disorder of WTe bundles, whereas the SdH oscillations are mainly derived from inner carriers away from the surface.

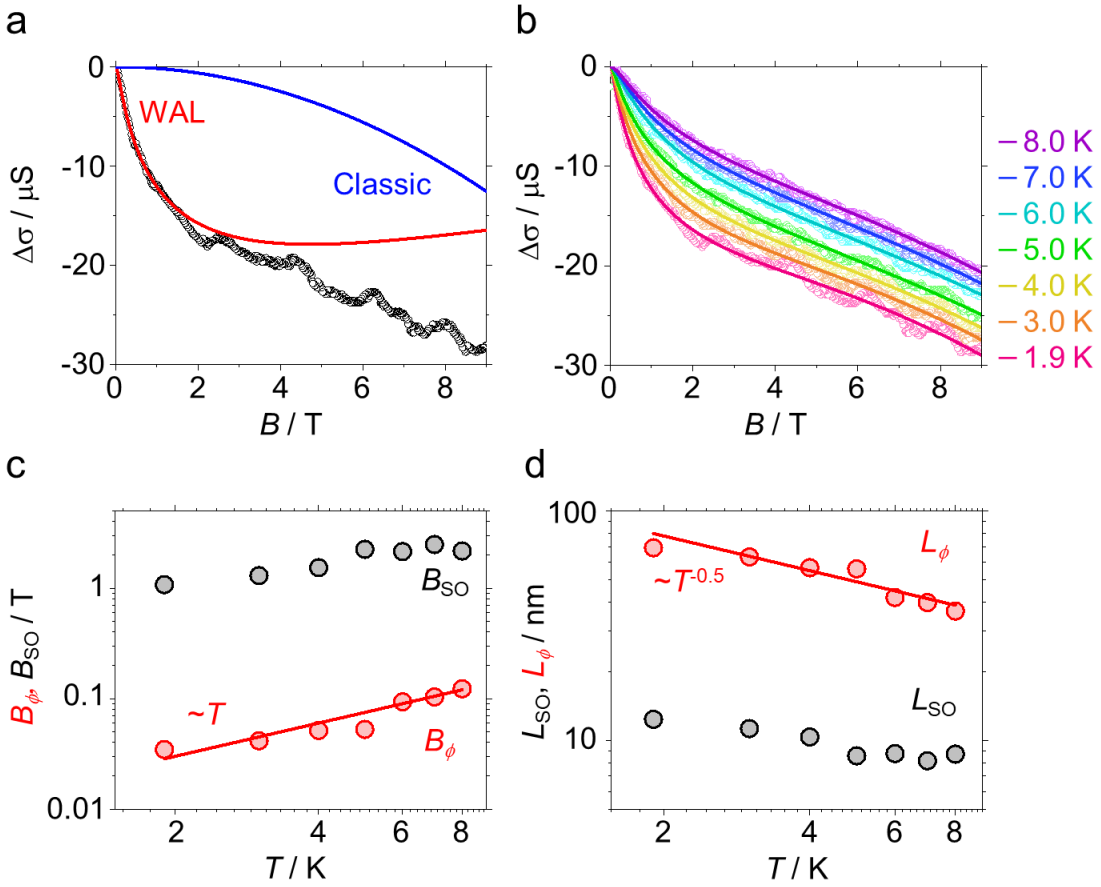


Figure 3.11 Comparison of measured Δσ (open circles) and fitting curves (solid lines) based on the Hikami−Larkin−Nagaoka theory and the classic MC of (a) 1.9 K and (b) 1.9 ~ 8 K. (c) Temperature dependence of $B\phi$ with the $T$ trend (red line) and $B$so. (d) Temperature dependence of $L\phi$ with the $T^{-0.5}$ trend (red line) and $L_{SO}$.

### 3.3.3 Band structure of WTe

To understand the origin of the SdH oscillations, the energy band structures and Fermi surface for a WTe bundle were calculated based on DFT. Figures 3.12a and b show the band dispersion relations along the ΓZ and YΓB directions, which are almost the same as the results reported in our previous study[23]. Here, the ΓZ and YΓB directions correspond to the directions parallel and perpendicular to the wire axis, respectively. There are two (three) bands passing through the Fermi level in the ΓZ and ΓY (ΓB) directions. Here, we consider the 2D Fermi surface on the ΓZ-ΓB plane, as shown in Figure 3.12c. There is one electron Fermi surface (cyan line around the Γ point) and two hole Fermi surfaces (magenta line around the Γ point and orange line around the B point). These carriers could contribute to the SdH oscillations observed for the laterally assembled WTe bundles. From the experimental SdH oscillation period, the cross-sectional area of the Fermi surface, $S_F$, is obtained as $2\times10^{-3}$ Å$^{-2}$ using the relation $S_F = 2\pi ef/\hbar$ [104]. This value is closest to the $S_F$ of the hole Fermi surface around the B point

($6\times10^{-2}$ Å$^{-2}$), although the value is approximately 1/30 of the calculated $S_F$. This difference is probably due to the DFT calculations being conducted for a 3D monoclinic crystal of a WTe bundle, whereas the SdH oscillations were measured for 2D-like films of WTe bundles. Note that observing the SdH oscillations derived from the other two Fermi surfaces under the magnetic field used in this study is difficult because their oscillation frequencies are expected to be higher. Therefore, to analyze multiple oscillations in detail, future research must be aimed at understanding the oscillations at higher magnetic fields.

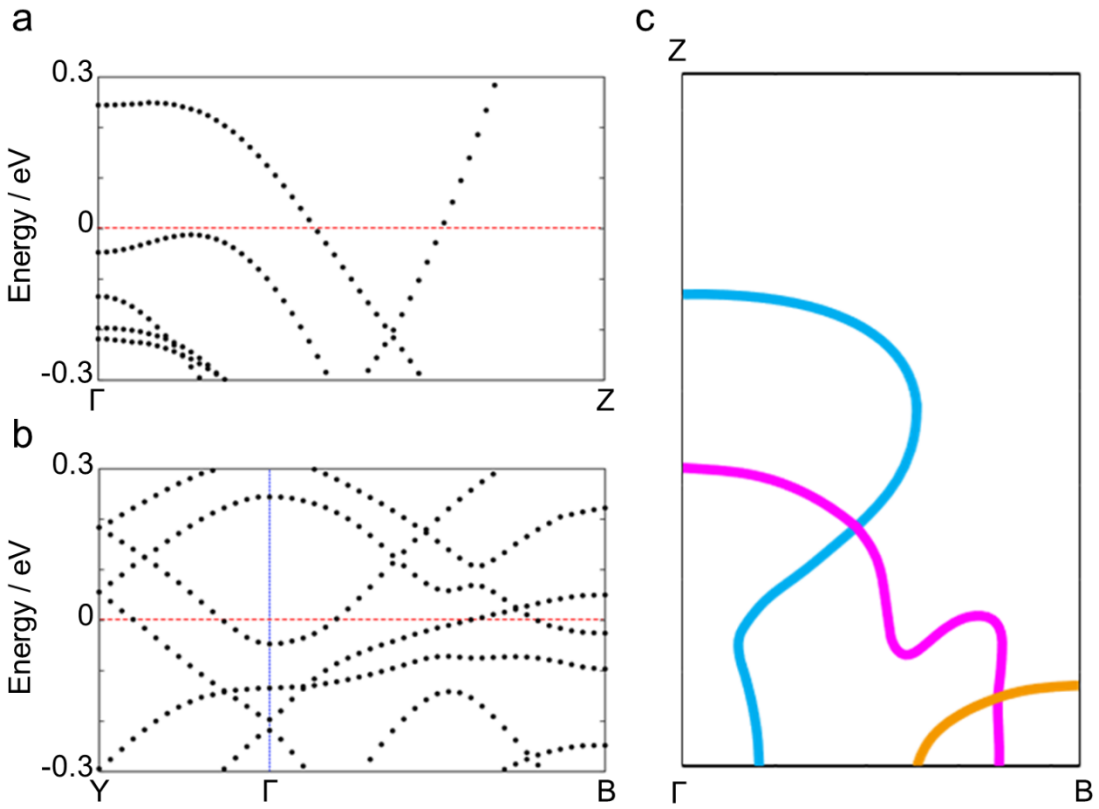


Figure 3.12 Electronic band structures. DFT-calculated band structures along the (a) Γ-Z and (b) Y-Γ-B lines, and (c) Fermi surface of a WTe bundle. The Fermi level is set to zero as a reference in (a) and (b). In (c), there is one electron Fermi surface (cyan line) and two hole Fermi surfaces (magenta and orange lines).

Finally, we discuss the validity of 2D carrier gas formation in a single bundle of laterally assembled WTe nanowires. DFT calculations revealed that the electronic bands for a 3D crystal of WTe wires have strong dispersion not only in the direction parallel to (ΓZ direction) but also in the direction perpendicular to (YΓB direction) the wire axis (Figures 3.12a and b). This also means that there is strong hybridization of the wave functions for the 5d orbitals of W and the 5p orbitals of Te between adjacent wires, as discussed in our previous study[23]. In more detail, the conduction and valence bands near the Fermi level are mainly derived from the Te 5p orbitals and from mixed contributions of both the W (5d) and Te (5p) orbitals, respectively. In particular, the Te 5p orbitals extend perpendicular to the wire axis. This enhances the electronic coupling of individual wires and contributes to the formation of a 2D carrier gas through hybridization of wave functions. This hybridization generates sufficient band dispersion with a typical width of approximately 0.3 eV in the perpendicular direction, even for the monolayer and bilayer WTe wire array[23]. This width is comparable to that in the direction parallel to the wire axis. For the networks of WTe bundles, this leads to metallic transport properties due to the low interwire contact resistance[23]. In the present study, individual wires aligned in bundles with high crystallinity were confirmed by STEM observations (Figure 3.4 (a−c)), which allows sufficiently high interwire interactions enabling electrons to move between wires. Furthermore, the thickness of ca. 10 nm also results in the formation of a 2D carrier gas in the present WTe bundles.

## 3.4 Conclusion

In conclusion, we have prepared long, ribbon-shaped aggregates of WTe nanowires as an unconventional 2D electronic system constructed using 1D vdW building blocks and have investigated their carrier transport properties. The formation of a 2D carrier gas in such laterally assembled WTe nanowires was confirmed by the angle-dependent SdH oscillations under a magnetic field. Importantly, SdH oscillations had never been observed in our previous study on networks of highly dense bundles of WTe wires[23]. The present work demonstrates the conversion of 1D to 2D electronic transport properties depending on the macroscopic aggregation state of the WTe nanowires. Controlling the aggregation state provides a tunable system to study the crossover phenomena not only from 1D to 2D systems but also to 3D systems. Notably, the present ribbon-shaped 2D systems should be different from conventional ribbon structures such as graphene and TMDCs. Because the wire-based nanoribbons consist solely of individual wires with vdW surfaces, we can ignore the edge structure and dangling bonds, which usually dominate the electronic properties and carrier scattering of conventional nanoribbons formed by covalent bonds. In other words, the structural defects and adsorbed impurities on the WTe surface could be the main factors for carrier scattering. These key features are highly useful for studying the size effects on the physical properties of low-dimensional electronic systems in the quantum limit. Furthermore, the aggregates of nanowires will provide an opportunity for intercalation into the interwire vdW space, resulting in modulation of the interwire

interaction and carrier density. The electronic properties and aggregation morphology of WTe wires can be further tuned by the chemical composition and growth conditions, respectively, because the importance of such factors has been demonstrated for the similar system of layered $WTe_2$[105-107]. Our findings have illustrated the versatility of TMC nanowires as ideal building blocks to explore the width- and layer number-dependent physical properties. As such, this will contribute to an understanding of the fundamental science of 1D vdW systems and dimensional crossover properties and to their application through material engineering.

# Chapter 4
# Conclusion

In this study, the interplay between the morphology and electronic states of $W_6Te_6$ nanofiber was explored through measurements of their electrical transport properties and magnetoresistance. Results from measurements of various network samples revealed both metallic and insulating properties. Comparisons with previous studies of $Li_2Mo_6Se_6$ nanofibers suggest that $W_6Te_6$ also displays electron transport properties that are influenced by the size of the nanofibers. The metallic network samples showed a more pronounced decrease in electrical resistance at low temperatures compared to previous studies of $Mo_6Te_6$ nanofiber networks synthesized by CVD. These results may indicate the higher crystallinity and distinct fiber aggregation states of the samples used in this study.

To gain a more in-depth understanding of the relationship between the morphology and electronic states, the electronic transport properties of a single $W_6Te_6$ nanofiber were investigated. The synthesis conditions for the CVD process were optimized, enabling the fabrication of even longer and more crystalline nanofibers by heating the growth substrate at higher temperatures. The electronic transport properties of the resulting ribbon-like $W_6Te_6$ nanofiber showed similar metallic behavior to that of the network samples. Magnetoresistance measurements observed that the magnetoresistance of a single $W_6Te_6$ nanofiber increases with magnetic field at low temperatures and also showed a distinct oscillatory structure. The geometry of these ribbon-like nanofibers suggests that these oscillations are SdH oscillations caused by 2D distributed electrons. Further investigation through measurements of magnetoresistance and the angular dependence of magnetic field and sample confirmed that the oscillation peaks depended on the perpendicular component of the magnetic field. These results strongly suggest that the oscillations were a result of the cyclotron motion of 2D carrier gas formed within the $W_6Te_6$ nanofibers. The monotonic increase in magnetoresistance with magnetic field suggests that the weak antilocalization (WAL) effect involving spin-orbit coupling was relatively stronger than the contribution of classical metal magnetoresistance due to the low dimensionality of the system. The analysis of the WAL effect revealed trends in magnetotransport properties of $W_6Te_6$ that are similar to other 2D electron systems, and ab initio calculations of the energy bands of $W_6Te_6$ further supported the formation of 2D electron systems in $W_6Te_6$ nanofibers.

This study represents the first experimental demonstration of TMC nanowires exhibiting 2D electron transport properties and suggests that TMC nanowires can be utilized to form electronic systems in various dimensional regions and study their physical properties by controlling their aggregation state.

## Acknowledgements

I would like to express my deepest gratitude to the many people who provided guidance, cooperation, and valuable advice during my research. First and foremost, I would like to thank my supervisor, Assoc. Prof. Yasumitsu Miyata, for his guidance and advice on various interesting research topics, experimental methods, and results, as well as his support during discussions and the writing of my doctoral dissertation. Over the course of my six-year research career, he not only provided valuable academic support, but also took care of my personal life and health outside of research. I am truly grateful for his support and take this opportunity to express my sincere appreciation. I would like to express my sincere appreciation to Asst. Prof. Yusuke Nakanishi, Asst. Prof. Hong En Lim, and Dr. Zhang Wenjin for their many helpful suggestions regarding my research. I am also grateful for the cooperation of many collaborators, without whom this research could not have been conducted. I would like to thank Mr. Takahiko Endo of our laboratory for providing the TMC samples used in this study, Prof. Taishi Takenobu, Asst. Prof. Jiang Pu, Mr. Shunichiro Ito, and Mr. Iori Kikuchi of Nagoya University, Dr. Yugo Oshima of RIKEN, Dr. Toshifumi Irisawa, and Dr. Naoya Okada of AIST for assisting with the measurement of electrical transport properties. In addition, Prof. Kazuhiro Yanagi of Tokyo Metropolitan University helped with sample fabrication. I am also indebted to Dr. Zheng Liu of AIST for observing HAADF-STEM images, and to Prof. Susumu Okada and Asst. Prof. Mina Maruyama of Tsukuba University for their energy band calculations. I am grateful not only for their cooperation, but also for their valuable advice and guidance during our research.

In addition, everyone in the Nanoscience Research Laboratory provided me with not only advice on my research, but also support in my daily life. My time with all of you in the laboratory has been a great source of emotional support and joy. I would like to take this opportunity to express my deepest gratitude. I would also like to thank my secretaries, Ms. Nonaka, Ms. Yamada, and Ms. Iwamoto, as well as the staff for their assistance in numerous ways.

Finally, I am grateful to my father, mother, sister, and friends who have supported me both physically and mentally throughout my journey. Thanks to all of you for your unwavering support and encouragement, I have been able to lead a fulfilling research life. I hope to continue pioneering new physical properties and physical phenomena, and to contribute to the advancement of nanophysics research.

# List of Publications

## Main publications

1.” Formation of a Two-Dimensional Electronic System in Laterally Assembled WTe Nanowires”
**Hiroshi Shimizu**, Jiang Pu, Zheng Liu, Hong En Lim, Mina Maruyama, Yusuke Nakanishi, Shunichiro Ito, Iori Kikuchi, Takahiko Endo, Kazuhiro Yanagi, Yugo Oshima, Susumu Okada, Taishi Takenobu, and Yasumitsu Miyata
*ACS Appl. Nano Mater.* **5**, (2022), 6277–6284

## Reference publications

1.” Vapor-Phase Indium Intercalation in van der Waals Nanofibers of Atomically Thin $W_6Te_6$ Wires”
Ryusuke Natsui, **Hiroshi Shimizu**, Yusuke Nakanishi, Zheng Liu, Nguyen Tuan Hung, Yung-Chang Lin, Akito Shimamura, Takahiko Endo, Jiang Pu, Iori Kikuchi, Taishi Takenobu, Susumu Okada, Kazu Suenaga, Riichiro Saito, and Yasumitsu Miyata
*ACS Nano* accepted

2.” Wafer-Scale Growth of One-Dimensional Transition-Metal Telluride Nanowires”
Hong En Lim, Yusuke Nakanishi, Zheng Liu, Jiang Pu, Mina Maruyama, Takahiko Endo, Chisato Ando, **Hiroshi Shimizu**, Kazuhiro Yanagi, Susumu Okada, Taishi Takenobu, and Yasumitsu Miyata
*Nano Lett.* **21**, (2021), 243–249

3.” Nanowire-to-Nanoribbon Conversion in Transition-Metal Chalcogenides: Implications for One-Dimensional Electronics and Optoelectronics”
Hong En Lim, Zheng Liu, Juan Kim, Jiang Pu, **Hiroshi Shimizu**, Takahiko Endo, Yusuke Nakanishi, Taishi Takenobu, and Yasumitsu Miyata
*ACS Appl. Nano Mater.* **5**, (2022), 1775–1782

4.” Versatile Post-Doping toward Two- Dimensional Semiconductors”
Yuya Murai, Shaochun Zhang, Takato Hotta, Zheng Liu, Takahiko Endo, **Hiroshi Shimizu**, Yasumitsu Miyata, Toshifumi Irisawa, Yanlin Gao, Mina Maruyama, Susumu Okada, Hiroyuki Mogi, Tomohiro Sato, Shoji Yoshida, Hidemi Shigekawa, Takashi Taniguchi, Kenji Watanabe, Ruben Canton-Vitoria, and Ryo Kitaura
*ACS Nano* **15**, (2021), 19225–19232

# Bibliography

(1) Novoselov, K. S.; Geim, A. K.; Morozov, S. V.; Jiang, D.; Katsnelson, M. I.; Grigorieva, I. V.; Dubonos, S. V.; Firsov, A. A., Two-dimensional gas of massless Dirac fermions in graphene. *Nature* **2005,** *438*, 197-200.

(2) Zhang, Y.; Tan, Y.-W.; Stormer, H. L.; Kim, P., Experimental observation of the quantum Hall effect and Berry's phase in graphene. *Nature* **2005,** *438*, 201-204.

(3) Novoselov, K. S.; Geim, A. K.; Morozov, S. V.; Jiang, D.; Zhang, Y.; Dubonos, S. V.; Grigorieva, I. V.; Firsov, A. A., Electric Field Effect in Atomically Thin Carbon Films. *Science* **2004,** *306*, 666-669.

(4) Novoselov, K. S.; Jiang, D.; Schedin, F.; Booth, T. J.; Khotkevich, V. V.; Morozov, S. V.; Geim, A. K., Two-dimensional atomic crystals. *Proceedings of the National Academy of Sciences* **2005,** *102*, 10451-10453.

(5) Geim, A. K.; Grigorieva, I. V., Van der Waals heterostructures. *Nature* **2013,** *499*, 419-425.

(6) Liu, Y.; Weiss, N. O.; Duan, X.; Cheng, H.-C.; Huang, Y.; Duan, X., Van der Waals heterostructures and devices. *Nature Reviews Materials* **2016,** *1*, 16042.

(7) Rao, R.; Pint, C. L.; Islam, A. E.; Weatherup, R. S.; Hofmann, S.; Meshot, E. R.; Wu, F.; Zhou, C.; Dee, N.; Amama, P. B.; Carpena-Nuñez, J.; Shi, W.; Plata, D. L.; Penev, E. S.; Yakobson, B. I.; Balbuena, P. B.; Bichara, C.; Futaba, D. N.; Noda, S.; Shin, H.; Kim, K. S.; Simard, B.; Mirri, F.; Pasquali, M.; Fornasiero, F.; Kauppinen, E. I.; Arnold, M.; Cola, B. A.; Nikolaev, P.; Arepalli, S.; Cheng, H.-M.; Zakharov, D. N.; Stach, E. A.; Zhang, J.; Wei, F.; Terrones, M.; Geohegan, D. B.; Maruyama, B.; Maruyama, S.; Li, Y.; Adams, W. W.; Hart, A. J., Carbon Nanotubes and Related Nanomaterials: Critical Advances and Challenges for Synthesis toward Mainstream Commercial Applications. *ACS Nano* **2018,** *12*, 11756-11784.

(8) Bockrath, M.; Cobden, D. H.; Lu, J.; Rinzler, A. G.; Smalley, R. E.; Balents, L.; McEuen, P. L., Luttinger-liquid behaviour in carbon nanotubes. *Nature* **1999,** *397*, 598-601.

(9) Ishii, H.; Kataura, H.; Shiozawa, H.; Yoshioka, H.; Otsubo, H.; Takayama, Y.; Miyahara, T.; Suzuki, S.; Achiba, Y.; Nakatake, M.; Narimura, T.; Higashiguchi, M.; Shimada, K.; Namatame, H.; Taniguchi, M., Direct observation of Tomonaga–Luttinger-liquid state in carbon nanotubes at low temperatures. *Nature* **2003,** *426*, 540-544.

(10) Shi, Z.; Hong, X.; Bechtel, H. A.; Zeng, B.; Martin, M. C.; Watanabe, K.; Taniguchi, T.; Shen, Y.-R.; Wang, F., Observation of a Luttinger-liquid plasmon in metallic single-walled carbon nanotubes. *Nature Photonics* **2015,** *9*, 515-519.

(11) Wang, S.; Wu, F.; Zhao, S.; Watanabe, K.; Taniguchi, T.; Zhou, C.; Wang, F., Logarithm Diameter Scaling and Carrier Density Independence of One-Dimensional Luttinger Liquid Plasmon. *Nano Letters* **2019,** *19*, 2360-2365.

(12) Wang, S.; Zhao, S.; Shi, Z.; Wu, F.; Zhao, Z.; Jiang, L.; Watanabe, K.; Taniguchi, T.; Zettl, A.; Zhou, C.; Wang, F., Nonlinear Luttinger liquid plasmons in semiconducting single-walled carbon nanotubes.

*Nature Materials* **2020,** *19*, 986-991.

(13) Zhao, S.; Wang, S.; Wu, F.; Shi, W.; Utama, I. B.; Lyu, T.; Jiang, L.; Su, Y.; Wang, S.; Watanabe, K.; Taniguchi, T.; Zettl, A.; Zhang, X.; Zhou, C.; Wang, F., Correlation of Electron Tunneling and Plasmon Propagation in a Luttinger Liquid. *Physical Review Letters* **2018,** *121*, 047702.

(14) Venkataraman, L.; Lieber, C. M., Molybdenum Selenide Molecular Wires as One-Dimensional Conductors. *Physical Review Letters* **1999,** *83*, 5334-5337.

(15) Venkataraman, L.; Hong, Y. S.; Kim, P., Electron Transport in a Multichannel One-Dimensional Conductor: Molybdenum Selenide Nanowires. *Physical Review Letters* **2006,** *96*, 076601.

(16) Kibsgaard, J.; Tuxen, A.; Levisen, M.; Lægsgaard, E.; Gemming, S.; Seifert, G.; Lauritsen, J. V.; Besenbacher, F., Atomic-Scale Structure of $Mo_6S_6$ Nanowires. *Nano Letters* **2008,** *8*, 3928-3931.

(17) Lin, J.; Cretu, O.; Zhou, W.; Suenaga, K.; Prasai, D.; Bolotin, K. I.; Cuong, N. T.; Otani, M.; Okada, S.; Lupini, A. R.; Idrobo, J.-C.; Caudel, D.; Burger, A.; Ghimire, N. J.; Yan, J.; Mandrus, D. G.; Pennycook, S. J.; Pantelides, S. T., Flexible metallic nanowires with self-adaptive contacts to semiconducting transition-metal dichalcogenide monolayers. *Nature Nanotechnology* **2014,** *9*, 436-442.

(18) Zhu, H.; Wang, Q.; Zhang, C.; Addou, R.; Cho, K.; Wallace, R. M.; Kim, M. J., New $Mo_6Te_6$ Sub-Nanometer-Diameter Nanowire Phase from 2H-$MoTe_2$. *Advanced Materials* **2017,** *29*, 1606264.

(19) Nagata, M.; Shukla, S.; Nakanishi, Y.; Liu, Z.; Lin, Y.-C.; Shiga, T.; Nakamura, Y.; Koyama, T.; Kishida, H.; Inoue, T.; Kanda, N.; Ohno, S.; Sakagawa, Y.; Suenaga, K.; Shinohara, H., Isolation of Single-Wired Transition-Metal Monochalcogenides by Carbon Nanotubes. *Nano Letters* **2019,** *19*, 4845-4851.

(20) Deng, J.; Huo, D.; Bai, Y.; Guo, Y.; Pan, Z.; Lu, S.; Cui, P.; Zhang, Z.; Zhang, C., Precise Tuning of Band Structures and Electron Correlations by van der Waals Stacking of One-dimensional $W_6Te_6$ Wires. *Nano Letters* **2020,** *20*, 8866-8873.

(21) Kanda, N.; Nakanishi, Y.; Liu, D.; Liu, Z.; Inoue, T.; Miyata, Y.; Tománek, D.; Shinohara, H., Efficient growth and characterization of one-dimensional transition metal tellurides inside carbon nanotubes. *Nanoscale* **2020,** *12*, 17185-17190.

(22) Xia, Y.; Wang, B.; Zhang, J.; Jin, Y.; Tian, H.; Ho, W.; Xu, H.; Jin, C.; Xie, M., Quantum Confined Tomonaga–Luttinger Liquid in $Mo_6Se_6$ Nanowires Converted from an Epitaxial $MoSe_2$ Monolayer. *Nano Letters* **2020,** *20*, 2094-2099.

(23) Lim, H. E.; Nakanishi, Y.; Liu, Z.; Pu, J.; Maruyama, M.; Endo, T.; Ando, C.; Shimizu, H.; Yanagi, K.; Okada, S.; Takenobu, T.; Miyata, Y., Wafer-Scale Growth of One-Dimensional Transition-Metal Telluride Nanowires. *Nano Letters* **2021,** *21*, 243-249.

(24) Yu, Y.; Wang, G.; Tan, Y.; Wu, N.; Zhang, X.-A.; Qin, S., Phase-Controlled Growth of One-Dimensional $Mo_6Te_6$ Nanowires and Two-Dimensional $MoTe_2$ Ultrathin Films Heterostructures. *Nano Letters* **2018,** *18*, 675-681.

(25) Potel, M.; Chevrel, R.; Sergent, M.; Armici, J. C.; Decroux, M.; Fischer, O., New pseudo-one-dimensional metals: $M_2Mo_6Se_6$ (M = Na, In, K, TI), $M_2Mo_6S_6$ (M = K, Rb, Cs), $M_2Mo_6Te_6$ (M = In, TI).

*Journal of Solid State Chemistry* **1980,** *35*, 286-290.

(26) Hönle, W.; Von Schnering, H. G.; Lipka, A.; Yvon, K., New compounds with infinite chains of face-condensed octahedral $Mo_6$ Clusters: $InMo_3Se_3$, $InMo_3Te_3$, $TlMo_3Se_3$ and $TlMo_3Te_3$. *Journal of the Less Common Metals* **1980,** *71*, 135-145.

(27) Potel, M.; Chevrel, R.; Sergent, M., Structure de $Tl_2Mo_9S_{11}$: clusters $Mo_{12}$ et $Mo_6$ isoles. *Acta Crystallographica Section B* **1980,** *36*, 1319-1322.

(28) Armici, J. C.; Decroux, M.; Fischer, Ø.; Potel, M.; Chevrel, R.; Sergent, M., A new pseudo-one-dimensional superconductor: $Tl_2Mo_6Se_6$. *Solid State Communications* **1980,** *33*, 607-611.

(29) Petrović, A. P.; Lortz, R.; Santi, G.; Decroux, M.; Monnard, H.; Fischer, Ø.; Boeri, L.; Andersen, O. K.; Kortus, J.; Salloum, D.; Gougeon, P.; Potel, M., Phonon mode spectroscopy, electron-phonon coupling, and the metal-insulator transition in quasi-one-dimensional $M_2Mo_6Se_6$. *Physical Review B* **2010,** *82*, 235128.

(30) Petrović, A. P.; Ansermet, D.; Chernyshov, D.; Hoesch, M.; Salloum, D.; Gougeon, P.; Potel, M.; Boeri, L.; Panagopoulos, C., A disorder-enhanced quasi-one-dimensional superconductor. *Nature Communications* **2016,** *7*, 12262.

(31) Gannon, L.; Boeri, L.; Howard, C. A.; Gougeon, P.; Gall, P.; Potel, M.; Salloum, D.; Petrović, A. P.; Hoesch, M., Lattice dynamics of the cluster chain compounds $M_2Mo_6Se_6$ ( M = K , Rb , Cs , In , and Tl ). *Physical Review B* **2018,** *98*, 014104.

(32) Nakayama, K.; Wang, Z.; Trang, C. X.; Souma, S.; Rienks, E. D. L.; Takahashi, T.; Ando, Y.; Sato, T., Observation of Dirac-like energy band and unusual spectral line shape in quasi-one-dimensional superconductor $Tl_2Mo_6Se_6$. *Physical Review B* **2018,** *98*, 140502.

(33) Wang, Z.; Zhang, X.; Jia, S., Physical properties of $TlFe_3Te_3$ near its first order transition. *Journal of Magnetism and Magnetic Materials* **2018,** *445*, 22-25.

(34) Guo, Z.; Sun, F.; Puggioni, D.; Luo, Y.; Li, X.; Zhou, X.; Chung, D. Y.; Cheng, E.; Li, S.; Rondinelli, J. M.; Yuan, W.; Kanatzidis, M. G., Local Distortions and Metal–Semiconductor–Metal Transition in Quasi-One-Dimensional Nanowire Compounds $AV_3Q_3O_\delta$ (A = K, Rb, Cs and Q = Se, Te). *Chemistry of Materials* **2021,** *33*, 2611-2623.

(35) Tessema, G. X.; Tseng, Y. T.; Skove, M. J.; Stillwell, E. P.; Brusetti, R.; Monceau, P.; Potel, M.; Gougeon, P., Stress-induced metal-to-nonmetal transition in the quasi-one-dimensional superconductor $Tl_2Mo_6Se_6$. *Physical Review B* **1991,** *43*, 3434-3437.

(36) Tseng, Y. T.; Tessema, G. X.; Skove, M. J.; Potel, M.; Gougeon, P., Metal to non metal transition in $Tl_2Mo_6Se_6$ under uniaxial stress: A study of the thermopower. *Solid State Communications* **1992,** *82*, 841-844.

(37) Zhang, F.; Wang, B.; Yin, H., $Ga_3Te_3I$: novel 1D and 2D semiconductor materials with promising electronic and optical properties. *Journal of Physics D Applied Physics* **2022,** *55*, 374005.

(38) Brusetti, R.; Briggs, A.; Laborde, O.; Potel, M.; Gougeon, P., Superconducting and dielectric

instabilities in $Tl_2Mo_6Se_6$: Unusual transport properties and unsaturating critical field. *Physical Review B* **1994,** *49*, 8931-8943.

(39) Davidson, P.; Gabriel, J. C.; Levelut, A. M.; Batail, P., A New Nematic Suspension Based on All-Inorganic Polymer Rods. *Europhysics Letters (EPL)* **1993,** *21*, 317-322.

(40) Chew, B. G. M.; Golden, J. H.; Huggins, B. A.; DiSalvo, F. J.; Zax, D. B., Probing the electronic structure in $M_2Mo_6Se_6$: Quadrupole couplings measured by NMR. *Physical Review B* **1994,** *50*, 7966-7976.

(41) Tarascon, J. M.; DiSalvo, F. J.; Murphy, D. W.; Hull, G.; Waszczak, J. V., New superconducting ternary molybdenum chalcogenides $InMo_6Se_8$, $TlMo_6S_8$, and $TlMo_6Se_8$. *Physical Review B* **1984,** *29*, 172-180.

(42) Tarascon, J. M.; DiSalvo, F. J.; Waszczak, J. V., Physical properties of several $M_2Mo_6X_6$ compounds (M = GROUP IA METAL; X = Se, Te). *Solid State Communications* **1984,** *52*, 227-231.

(43) Tarascon, J. M.; Hull, G. W.; DiSalvo, F. J., A facile synthesis of pseudo one-monodimensional ternary molybdenum chalcogenides $M_2Mo_6X_6$ (X = Se,Te; M = Li,Na..Cs). *Materials Research Bulletin* **1984,** *19*, 915-924.

(44) Tarascon, J. M.; DiSalvo, F. J.; Chen, C. H.; Carroll, P. J.; Walsh, M.; Rupp, L., First example of monodispersed $(Mo_3Se_3)^1{}_\infty$ clusters. *Journal of Solid State Chemistry* **1985,** *58*, 290-300.

(45) Tarascon, J. M., $Mo_6Se_6$: A New Solid‐State Electrode for Secondary Lithium Batteries. *Journal of The Electrochemical Society* **1985,** *132*, 2089.

(46) Sheridan, J. G.; Heidelberg, A.; Brougham, D. F.; Nellist, P. D.; Langford, R. M.; Boland, J. J., Self-Assembly of $LiMo_3Se_3$ Nanowire Networks from Nanoscale Building-Blocks in Solution. *Langmuir* **2012,** *28*, 15344-15349.

(47) Jeon, J.; Oh, S.; Choi, K. H.; Chae, S.; Woo, C.; Dong, X.; Asghar, G.; Ahn, J.; Kim, T. Y.; Ali, J.; Yu, H. K.; Choi, J.-Y., Synthesis of one-dimensional atomic chain $LiMo_3Se_3$ through ion-exchange reaction from $InMo_3Se_3$: Kinetics and thermodynamics. *Ceramics International* **2021,** *47*, 33606-33610.

(48) Dronskowski, R.; Hoffmann, R., Bond reactivities, acidities, and basicities within $AMo_3X_3$ phases (A = Li, Na, K, In; X = Se, Te). *Inorganic Chemistry* **1992,** *31*, 3107-3113.

(49) Golden, J. H.; DiSalvo, F. J.; Frechet, J. M. J., Ordered Conducting Films of the Inorganic Polymer $(LiMo_3Se_3)_n$ Cast From Solution. *Chemistry of Materials* **1995,** *7*, 232-235.

(50) Golden, J. H.; DiSalvo, F. J.; Fréchet, J. M. J.; Silcox, J.; Thomas, M.; Elman, J., Subnanometer-Diameter Wires Isolated in a Polymer Matrix by Fast Polymerization. *Science* **1996,** *273*, 782-784.

(51) Osterloh, F. E.; Martino, J. S.; Hiramatsu, H.; Hewitt, D. P., Stringing up the Pearls: Self-Assembly, Optical and Electronic Properties of CdSe− and Au−$LiMo_3Se_3$ Nanoparticle−Nanowire Composites. *Nano Letters* **2003,** *3*, 125-129.

(52) Qi, X.; Osterloh, F. E., Chemical Sensing with $LiMo_3Se_3$ Nanowire Films. *Journal of the American Chemical Society* **2005,** *127*, 7666-7667.

(53) Qi, X.; Osterloh, F. E.; Barriga, S. A.; Giacomo, J. A.; Chiang, S., Molecular Adsorption to

$LiMo_3Se_3$ Nanowire Film Chemiresistors. *Analytical Chemistry* **2006,** *78*, 1306-1311.

(54) Brusetti, R.; Monceau, P.; Potel, M.; Gougeon, P.; Sergent, M., The exotic superconductor $Tl_2Mo_6Se_6$ investigated by low field magnetization measurements. *Solid State Communications* **1988,** *66*, 181-187.

(55) Brusetti, R.; Dianoux, A. J.; Gougeon, P.; Potel, M.; Bonjour, E.; Calemczuk, R., Phonon density of states of the quasi-one-dimensional molybdenum selenides $M_2Mo_6Se_6$ (M=Tl, In, Rb, and vacancy): Evidence of Einstein-like M-atom modes in the superconducting compounds. *Physical Review B* **1990,** *41*, 6315-6320.

(56) Huang, S. Z.; Mayerle, J. J.; Greene, R. L.; Wu, M. K.; Chu, C. W., Pressure dependence of superconductivity in the pseudo-one-dimensional compound $Tl_2Mo_6Se_6$. *Solid State Communications* **1983,** *45*, 749-751.

(57) Mori, T.; Yokogawa, Y.; Kobayashi, A.; Sasaki, Y.; Kobayashi, H., Thermoelectricity of pseudo-one-dimensional ternary chalcogenides: $Tl_2Mo_6Se_6$ and $In_2Mo_6Se_6$. *Solid State Communications* **1984,** *49*, 249-252.

(58) Lepetit, R.; Monceau, P.; Potel, M.; Gougeon, P.; Sergent, M., Superconductivity of the linear chain compound $Tl_2Mo_6Se_6$. *Journal of Low Temperature Physics* **1984,** *56*, 219-235.

(59) Hor, P. H.; Fan, W. C.; Chou, L. S.; Meng, R. L.; Chu, C. W.; Tarascon, J. M.; Wu, M. K., Study of the metal-semiconductor transition in $Rb_2Mo_6Se_6$, $Rb_2Mo_6Te_6$ and $Cs_2Mo_6Te_6$ under pressures. *Solid State Communications* **1985,** *55*, 231-235.

(60) Cai, S.-H.; Liu, C.-W., Theoretical investigation on the band structures of several Chevrel-phase compounds. *Journal of the Chemical Society, Faraday Transactions* **1995,** *91*, 479-483.

(61) Çakır, D.; Durgun, E.; Gülseren, O.; Ciraci, S., First principles study of electronic and mechanical properties of molybdenum selenide type nanowires. *Physical Review B* **2006,** *74*, 235433.

(62) Gemming, S.; Seifert, G.; Vilfan, I., Li doped $Mo_6S_6$ nanowires: elastic and electronic properties. *physica status solidi (b)* **2006,** *243*, 3320-3324.

(63) Liu, Q.; Zunger, A., Predicted Realization of Cubic Dirac Fermion in Quasi-One-Dimensional Transition-Metal Monochalcogenides. *Physical Review X* **2017,** *7*, 021019.

(64) Yang, T.; Zhang, X., Nearly flat nodal surface states in pseudo-one-dimensional molybdenum monochalcogenides $X(MoS)_3$ (X = K, Rb, and Cs). *Journal of Materials Chemistry C* **2020,** *8*, 9046-9054.

(65) Song, Z.; Li, B.; Xu, C.; Wu, S.; Qian, B.; Chen, T.; Biswas, P. K.; Xu, X.; Sun, J., Pressure engineering of the Dirac fermions in quasi-one-dimensional $Tl_2Mo_6Se_6$. *Journal of Physics: Condensed Matter* **2020,** *32*, 215402.

(66) Popov, I.; Gemming, S.; Okano, S.; Ranjan, N.; Seifert, G., Electromechanical Switch Based on Mo6S6 Nanowires. *Nano Letters* **2008,** *8*, 4093-4097.

(67) Neal, A. T.; Du, Y.; Liu, H.; Ye, P. D., Two-Dimensional $TaSe_2$ Metallic Crystals: Spin–Orbit Scattering Length and Breakdown Current Density. *ACS Nano* **2014,** *8*, 9137-9142.

(68) Li, H.; Peng, Y.; Teng, J.; Cao, J., Study on the electronic properties of $M_6X_6$ (M = Mo, W; X = S, Se, Te) nanowire arrays. *Chemical Physics Letters* **2021,** *780*, 138905.

(69) Murugan, P.; Kumar, V.; Kawazoe, Y.; Ota, N., Lithiated assemblies of metal chalcogenide nanowires. *Applied Physics Letters* **2008,** *92*, 203112.

(70) Yang, X.; Xian, J.-J.; Li, G.; Nagaosa, N.; Zhang, W.-H.; Qin, L.; Zhang, Z.-M.; Lü, J.-T.; Fu, Y.-S., Possible Phason-Polaron Effect on Purely One-Dimensional Charge Order of $Mo_6Se_6$ Nanowires. *Physical Review X* **2020,** *10*, 031061.

(71) Shimizu, H.; Pu, J.; Liu, Z.; Lim, H. E.; Maruyama, M.; Nakanishi, Y.; Ito, S.; Kikuchi, I.; Endo, T.; Yanagi, K.; Oshima, Y.; Okada, S.; Takenobu, T.; Miyata, Y., Formation of a Two-Dimensional Electronic System in Laterally Assembled WTe Nanowires. *ACS Applied Nano Materials* **2022,** *5*, 6277-6284.

(72) Slade, C. A.; Sanchez, A. M.; Sloan, J., Unprecedented New Crystalline Forms of SnSe in Narrow to Medium Diameter Carbon Nanotubes. *Nano Letters* **2019,** *19*, 2979-2984.

(73) Yoo, Y.; Jeong, J. S.; Ma, R.; Koester, S. J.; Johns, J. E., Ultrathin One-Dimensional Molybdenum Telluride Quantum Wires Synthesized by Chemical Vapor Deposition. *Chemistry of Materials* **2020,** *32*, 9650-9655.

(74) Hong, J.; Chen, X.; Li, P.; Koshino, M.; Li, S.; Xu, H.; Hu, Z.; Ding, F.; Suenaga, K., Multiple 2D Phase Transformations in Monolayer Transition Metal Chalcogenides. *Advanced Materials* **2022,** *34*, 2200643.

(75) Faulques, E.; Kalashnyk, N.; Slade, C. A.; Sanchez, A. M.; Sloan, J.; Ivanov, V. G., Vibrational and electronic structures of tin selenide nanowires confined inside carbon nanotubes. *Synthetic Metals* **2022,** *284*, 116968.

(76) Ribeiro, F. J.; Roundy, D. J.; Cohen, M. L., Electronic properties and ideal tensile strength of MoSe nanowires. *Physical Review B* **2002,** *65*, 153401.

(77) Vilfan, I., $Mo_6S_6$ nanowires: structural, mechanical and electronic properties. *The European Physical Journal B - Condensed Matter and Complex Systems* **2006,** *51*, 277-284.

(78) Popov, I.; Yang, T.; Berber, S.; Seifert, G.; Tománek, D., Unique Structural and Transport Properties of Molybdenum Chalcohalide Nanowires. *Physical Review Letters* **2007,** *99*, 085503.

(79) Zhang, W.; Wang, J.; Zhao, L.; Wang, J.; Zhao, M., Transition-metal monochalcogenide nanowires: highly efficient bi-functional catalysts for the oxygen evolution/reduction reactions. *Nanoscale* **2020,** *12*, 12883-12890.

(80) Jin, K.-H.; Liu, F., 1D topological phases in transition-metal monochalcogenide nanowires. *Nanoscale* **2020,** *12*, 14661-14667.

(81) Ying, P.; Zhang, J.; Zhou, J.; Liang, Q.; Zhong, Z., Mechanical behaviors of MoS nanowires under tension from molecular dynamics simulations. *Computational Materials Science* **2020,** *179*, 109691.

(82) Peng, Y.; Wei, X.; Jin, C.; Zhang, Y.; Cao, J., Strain induced structural phase transition in $TM_6X_6$

(TM = Mo, W; X = S, Se, Te) nanowires. *Journal of Solid State Chemistry* **2021,** *300*, 122194.

(83) Shang, C.; Fu, L.; Zhou, S.; Zhao, J., Atomic Wires of Transition Metal Chalcogenides: A Family of 1D Materials for Flexible Electronics and Spintronics. *JACS Au* **2021,** *1*, 147-155.

(84) Teng, J.; Cao, J.; Ouyang, T.; Yao, Y.; Chen, C.; Wei, X., Stability and electronic properties of α/β-$Mo_6S_6$ nanowires encapsulated inside carbon nanotubes. *Physica E: Low-dimensional Systems and Nanostructures* **2021,** *134*, 114891.

(85) Hoffmann, R.; Shaik, S.; Scott, J. C.; Whangbo, M.-H.; Foshee, M. J., The electronic structure of $NbSe_3$. *Journal of Solid State Chemistry* **1980,** *34*, 263-269.

(86) Hughbanks, T.; Hoffmann, R., Molybdenum chalcogenides: clusters, chains, and extended solids. The approach to bonding in three dimensions. *Journal of the American Chemical Society* **1983,** *105*, 1150-1162.

(87) Mu, Q.-G.; Ruan, B.-B.; Zhao, K.; Pan, B.-J.; Liu, T.; Shan, L.; Chen, G.-F.; Ren, Z.-A., Superconductivity at 10.4 K in a novel quasi-one-dimensional ternary molybdenum pnictide $K_2Mo_3As_3$. *Science Bulletin* **2018,** *63*, 952-956.

(88) Potel, M.; Chevrel, R.; Sergent, M.; Armici, J. C.; Decroux, M.; Fischer, Ø., New pseudo-one-dimensional metals: $M_2Mo_6Se_6$ (M = Na, In, K, TI), $M_2Mo_6S_6$ (M = K, Rb, Cs), $M_2Mo_6Te_6$ (M = In, TI). *Journal of Solid State Chemistry* **1980,** *35*, 286-290.

(89) Wang, L.; Gutiérrez-Lezama, I.; Barreteau, C.; Ubrig, N.; Giannini, E.; Morpurgo, A. F., Tuning magnetotransport in a compensated semimetal at the atomic scale. *Nature Communications* **2015,** *6*, 8892.

(90) Hohenberg, P.; Kohn, W., Inhomogeneous Electron Gas. *Physical Review* **1964,** *136*, B864-B871.

(91) Kohn, W.; Sham, L. J., Self-Consistent Equations Including Exchange and Correlation Effects. *Physical Review* **1965,** *140*, A1133-A1138.

(92) Morikawa, Y.; Iwata, K.; Terakura, K., Theoretical study of hydrogenation process of formate on clean and Zn deposited Cu(111) surfaces. *Applied Surface Science* **2001,** *169-170*, 11-15.

(93) Hamada, I., Simulation Tool for Atom TEchnology (STATE). *https://state-doc.readthedocs.io/en/latest/index.html*.

(94) Perdew, J. P.; Burke, K.; Ernzerhof, M., Generalized Gradient Approximation Made Simple. *Physical Review Letters* **1996,** *77*, 3865-3868.

(95) Vanderbilt, D., Soft self-consistent pseudopotentials in a generalized eigenvalue formalism. *Physical Review B* **1990,** *41*, 7892-7895.

(96) Woods, J. M.; Shen, J.; Kumaravadivel, P.; Pang, Y.; Xie, Y.; Pan, G. A.; Li, M.; Altman, E. I.; Lu, L.; Cha, J. J., Suppression of Magnetoresistance in Thin $WTe_2$ Flakes by Surface Oxidation. *ACS Applied Materials & Interfaces* **2017,** *9*, 23175-23180.

(97) Wu, Z.; Xu, S.; Lu, H.; Khamoshi, A.; Liu, G.-B.; Han, T.; Wu, Y.; Lin, J.; Long, G.; He, Y.; Cai, Y.; Yao, Y.; Zhang, F.; Wang, N., Even–odd layer-dependent magnetotransport of high-mobility Q-valley electrons in transition metal disulfides. *Nature Communications* **2016,** *7*, 12955.

(98) Fallahazad, B.; Movva, H. C. P.; Kim, K.; Larentis, S.; Taniguchi, T.; Watanabe, K.; Banerjee, S. K.; Tutuc, E., Shubnikov--de Haas Oscillations of High-Mobility Holes in Monolayer and Bilayer $WSe_2$: Landau Level Degeneracy, Effective Mass, and Negative Compressibility. *Physical Review Letters* **2016,** *116*, 086601.

(99) Hikami, S.; Larkin, A. I.; Nagaoka, Y., Spin-Orbit Interaction and Magnetoresistance in the Two Dimensional Random System. *Progress of Theoretical Physics* **1980,** *63*, 707-710.

(100) Altshuler, B. L.; Aronov, A. G.; Khmelnitsky, D. E., Effects of electron-electron collisions with small energy transfers on quantum localisation. *Journal of Physics C: Solid State Physics* **1982,** *15*, 7367.

(101) Liu, H.; Bao, L.; Zhou, Z.; Che, B.; Zhang, R.; Bian, C.; Ma, R.; Wu, L.; Yang, H.; Li, J.; Gu, C.; Shen, C.-M.; Du, S.; Gao, H.-J., Quasi-2D Transport and Weak Antilocalization Effect in Few-layered $VSe_2$. *Nano Letters* **2019,** *19*, 4551-4559.

(102) Roy, A.; Guchhait, S.; Sonde, S.; Dey, R.; Pramanik, T.; Rai, A.; Movva, H. C. P.; Colombo, L.; Banerjee, S. K., Two-dimensional weak anti-localization in $Bi_2Te_3$ thin film grown on Si(111)-(7 × 7) surface by molecular beam epitaxy. *Applied Physics Letters* **2013,** *102*, 163118.

(103) Schmidt, H.; Yudhistira, I.; Chu, L.; Castro Neto, A. H.; Özyilmaz, B.; Adam, S.; Eda, G., Quantum Transport and Observation of Dyakonov-Perel Spin-Orbit Scattering in Monolayer $MoS_2$. *Physical Review Letters* **2016,** *116*, 046803.

(104) Shoenberg, D., Magnetic Oscillations in Metals. *Cambridge University Press: Cambridge [Cambridgeshire]; New York,* **1984**.

(105) Deng, Y.; Li, P.; Zhu, C.; Zhou, J.; Wang, X.; Cui, J.; Yang, X.; Tao, L.; Zeng, Q.; Duan, R.; Fu, Q.; Zhu, C.; Xu, J.; Qu, F.; Yang, C.; Jing, X.; Lu, L.; Liu, G.; Liu, Z., Controlled Synthesis of $Mo_xW_{1-x}Te_2$ Atomic Layers with Emergent Quantum States. *ACS Nano* **2021,** *15*, 11526-11534.

(106) Li, P.; Deng, Y.; Hsu, C.-H.; Zhu, C.; Cui, J.; Yang, X.; Zhou, J.; Hung, Y.-C.; Fan, J.; Ji, Z.; Qu, F.; Shen, J.; Yang, C.; Jing, X.; Lin, H.; Liu, Z.; Lu, L.; Liu, G., Dimensionality-dependent type-II Weyl semimetal state in $Mo_{0.25}W_{0.75}Te_2$. *Physical Review B* **2021,** *104*, 085423.

(107) Xu, M.; Tang, B.; Lu, Y.; Zhu, C.; Lu, Q.; Zhu, C.; Zheng, L.; Zhang, J.; Han, N.; Fang, W.; Guo, Y.; Di, J.; Song, P.; He, Y.; Kang, L.; Zhang, Z.; Zhao, W.; Guan, C.; Wang, X.; Liu, Z., Machine Learning Driven Synthesis of Few-Layered $WTe_2$ with Geometrical Control. *Journal of the American Chemical Society* **2021,** *143*, 18103-18113.